Wave-induced mean currents and setup over barred and steep sandy beaches

Kévin Martins, Xavier Bertin, Baptiste Mengual, Marc Pezerat, Laura Lavaud, Thomas Guérin, Yinglong Zhang

HAL Id: hal-03817250

https://hal-univ-rochelle.archives-ouvertes.fr/hal-03817250

Submitted on 17 Oct 2022

Wave-induced mean currents and setup over barred and steep sandy beaches

Kévin Martins[a,*], Xavier Bertin[b], Baptiste Mengual[c], Marc Pezerat[b], Laura Lavaud[b], Thomas Guérin[c], Yinglong J. Zhang[d]

[a]*Univ. Bordeaux, CNRS, Bordeaux INP, EPOC, UMR 5805, F-33600 Pessac, France*
[b]*La Rochelle University, CNRS, LIENSs, UMRi 7266, 2 rue Olympe de Gouges, 17000 La Rochelle, France*
[c]*BW-CGC (Benoit Waeles - Consultant Génie Côtier); 53 rue du Commandant Groix, 29200 Brest, France.*
[d]*Virginia Institute of Marine Science, College of William & Mary, Gloucester Point, VA, 23062, USA*

Abstract

Wind-generated surface waves breaking in the nearshore cause an increase in mean water levels, the wave setup, which can represent a significant fraction of storm surges developing both along open coasts and over sheltered areas such as coastal lagoons and estuaries. A common way to simulate the wave setup is to assume a balance between the barotropic gradient and the divergence of the depth-integrated wave-averaged momentum flux (radiation stress) associated with breaking waves in the surf zone. Field observations collected at several sandy beaches revealed that this depth-integrated approach could largely underestimate the wave setup close to the shoreline (by up to a factor of 2). The present study builds on Guérin et al. (2018) and further investigates how representing the depth-varying wave-induced forcing in modelling systems can improve the prediction of wave setup across the surf zone. We use data collected during two major field campaigns at Duck, N.C., combined with simulations with SCHISM, a three-dimensional (3D) phase-averaged modelling system employing the vortex-force formalism to represent the effects of waves on currents. The ability of SCHISM to reproduce the surf zone circulation is first assessed with data collected during October 1994 (Duck94), which serve as a classical benchmark for 3D hydrostatic oceanic circulation models. The wave setup dynamics are then analysed during a storm event that occurred during SandyDuck. Consistent with the results of Guérin et al. (2018), we find that resolving the depth-varying nearshore circulation results in increased and improved wave setup predictions across the surf zone. At the shoreline, depth-integrated approaches based on the vortex-force formalism or the radiation stress concept underestimate the maximal wave setup by 10-15% and 30% on the 1:14 foreshore slope, respectively. An analysis of the 3D cross-shore momentum balance reveals that the vertical mixing is the second most important contributor (10-15% across the surf zone) to the simulated wave setup after the wave forces (80-90%), followed by the vertical advection whose contribution increases with the beach slope (up to 10% at the shoreline). Simulations performed with a phase-resolving numerical model suggest that the largest discrepancies observed at the shoreline in past studies likely originate from swash-related processes, highlighting the difficulties to disentangle wave and swash processes on steep foreshores in the field.

1. Introduction

As they break in the nearshore region, wind-generated surface gravity waves (hereafter short waves) generate currents at various temporal and spatial scales (*e.g.*, Svendsen, 1984a; Peregrine and Bokhove, 1998; Bühler and Jacobson, 2001; Smith, 2006; Castelle et al., 2016). The wave-driven nearshore circulation controls the short- to long-term morphological evolution of coastlines (Wright and Short, 1984) and plays an important role in the exchanges of nutrients and pollutants between the coastal region and the continental

*Corresponding author
Email address:* `kevin.martins@u-bordeaux.fr` (Kévin Martins)

shelf (Morgan et al., 2018). The excess of momentum due to breaking also causes an increase in mean water levels – the wave setup – that generally reaches its maximum close to the shoreline (*e.g.*, see Bowen et al., 1968; Guza and Thornton, 1981; Nielsen, 1988; Lentz and Raubenheimer, 1999). During storms, the wave setup can exceed 1 m at the coast, and hence greatly contributes to the storm surge observed along open coasts bordered by narrow to moderately-wide shelves (Fiedler et al., 2015; Guérin et al., 2018). Large waves breaking over ebb deltas also generate a setup that can extend at the scale of coastal lagoons or large estuaries (*e.g.*, see Malhadas et al., 2009; Olabarrieta et al., 2011; Fortunato et al., 2017; Lavaud et al., 2020), causing potential hazard to supposedly sheltered areas. The wave setup that develops along shorelines adjacent to tidal inlets exerts a key control on their morphodynamics. Indeed, the lateral barotropic pressure gradients associated with longshore-varying wave setup can drive strong flows and sediment transport oriented towards the lagoon (Bertin et al., 2009). The wave setup is also a component of the wave runup, which determines the maximal elevation under the action of waves. Developing a good understanding of wave breaking processes in the nearshore and how those lead to the wave setup is thus essential for improving our capacity to predict and mitigate coastal risks such as flooding and erosion.

Following the early observation-based studies on wave setup dynamics (Savage, 1957; Fairchild, 1958; Saville, 1961), Longuet-Higgins and Stewart introduced the concept of radiation stress – the excess flux of momentum due to the presence of waves – in order to describe the two-dimensional depth-averaged (2DH) forcing exerted by short waves on the water column (Longuet-Higgins and Stewart, 1962, 1964). In nearshore regions where the bottom stress is negligible (*i.e.*, weak current over smooth bottoms), a close balance was observed in the field between the time and depth-averaged wave momentum fluxes and the barotropic pressure gradient induced by the tilted mean water level either due to shoaling (setdown) or breaking (setup) waves (Guza and Thornton, 1981; Lentz and Raubenheimer, 1999; Raubenheimer et al., 2001):

$$\frac{\partial S_{xx}}{\partial x} \sim -\rho g h \frac{\partial \eta}{\partial x} \tag{1}$$

where S_{xx} is the cross-shore component of the radiation stress tensor (x being the cross-shore spatial coordinate), ρ is the water density, g is the gravity constant, η is the time-averaged (over several wave groups) surface elevation and h is the mean water depth. However, several studies reported that numerical models based on this simple balance (Eq. 1) could result in a substantial underestimation of the wave setup close to the shoreline (up to a factor of 2, *e.g.*, see Guza and Thornton, 1981; Raubenheimer et al., 2001; Apotsos et al., 2007), suggesting that other processes may be important. One of the reasons for this discrepancy in shallow water depths resides in the large onshore-directed bottom stress associated with intense undertows that develop under breaking and broken waves (Svendsen, 1984b; Deigaard et al., 1991), and which directly contributes to the wave setup (Apotsos et al., 2007). Using the same dataset as Raubenheimer et al. (2001) (SandyDuck experiments in 1997 at Duck, N.C.), Apotsos et al. (2007) could reduce the errors to within ~ 30% of the observations by including the effects from the shear stresses at the bottom estimated via a simple one-dimensional (along the vertical, 1DV) undertow model.

The radiation stress formalism embeds both adiabatic (*i.e.* conserving the wave momentum flux) and dissipative effects of short waves on currents, which complicates the physical interpretation of wave-current interactions. Following the ideas of Garrett (1976) in deep water, Smith (2006) decomposed the total momentum into mean current and surface wave components in order to derive an equivalent, but physically easier-to-interpret, formulation for the effects of short waves on currents in the nearshore region. This decomposition directly links the energy dissipation associated with breaking waves with the large scale vorticity observed in surf zones (Bonneton et al., 2010). The vortex-force (VF) formalism extends this approach to the vertical, and allows for the reproduction of depth-varying wave-induced circulation such as Langmuir cells in deep water (*e.g.* Leibovich, 1980) and nearshore currents (*e.g.*, Newberger and Allen, 2007a; Uchiyama et al., 2010; Kumar et al., 2012; Lavaud et al., 2022; Pezerat et al., 2022). Using the approximated Generalized Lagrangian Mean (GLM) equations derived by Ardhuin et al. (2008), Bennis

et al. (2011) proposed a set of equations for the depth-varying effects of short waves on currents which, when integrated over depth, are closely equivalent to those derived by Smith (2006). The depth-varying adiabatic terms of the equations of Bennis et al. (2011) are exact to second order in wave slope, however, the vertical shape of the dissipation terms are virtually unknown. In the case of depth-induced breaking for instance, the forcing is most often viewed as a surface stress (*e.g.,* Phillips, 1977; Deigaard, 1993; Walstra et al., 2000), but empirical shape functions based on local wave properties such as the dominant wavenumber have also been used in previous studies (*e.g.,* see Uchiyama et al., 2010). An adequate parametrisation for the vertical mixing is, in both cases, required for accurately representing the strongly sheared currents commonly observed in surf zones (Feddersen and Trowbridge, 2005; Uchiyama et al., 2010; Kumar et al., 2012; Delpey et al., 2014; Pezerat et al., 2022).

The VF formalism has now been implemented within several 3D hydrostatic oceanic circulation models, mostly based on the equations derived by McWilliams et al. (2004) using multiple asymptotic scale analyses (*e.g.* ROMS- or FVCOM-based models, see Uchiyama et al., 2010; Kumar et al., 2012; Zheng et al., 2017) or those derived by Ardhuin et al. (2008) from the GLM equations for the quasi-Eulerian current velocities of Andrews and McIntyre (1978). Closely equivalent approaches include the works of Newberger and Allen (2007a,b), implemented in POM. The equations of Bennis et al. (2011), simplified from Ardhuin et al. (2008) for the case of weakly sheared currents, were implemented in models such as SYMPHONIE (Michaud et al., 2012), GETM (Moghimi et al., 2013), MOHID (Delpey et al., 2014) and SCHISM (Guérin et al., 2018). Though depth-induced breaking processes remain crudely parametrised in phase-averaged models, the VF formalism substantially improved our capacity to realistically simulate the nearshore circulation and the vertically-sheared currents observed in surf zones compared to the previous 1DV modelling approaches (Svendsen, 1984a; Stive and Wind, 1986; Deigaard et al., 1991). Recent studies also brought strong evidence that resolving the depth-varying wave-driven circulation in the nearshore also influences wave setup estimates at the shoreline. Although their wave setup predictions were primarily controlled by the choice for the wave breaking index, Bennis et al. (2014) identified a relatively strong influence from the parametrisation of the bottom shear stress and the vertical mixing on the simulated wave setup (variations of about 10%). By combining field measurements collected on a dissipative sandy beach and numerical simulations with the three-dimensional (3D) phase-averaged modelling system SCHISM, Guérin et al. (2018) corroborated these findings and identified important contributions to the simulated wave setup from the depth-varying surf zone circulation (dominantly the horizontal advection and the vertical mixing). Using synthetic cases as in Bennis et al. (2014), these authors also suggested that this contribution increases with the beach slope (up to ~20% increase on 1:20 slopes), thus providing a potential explanation for the commonly-reported underestimations of wave setup predictions near the shoreline with 2DH modelling approaches (Apotsos et al., 2007).

The present study builds on Guérin et al. (2018) and aims to further analyse how representing the depth-varying surf zone circulation in 3D hydrostatic ocean modelling systems can affect and improve the predictions of wave setup on barred and steep sandy beaches. At the spatial scales considered in this study, the wave setup dynamics is often analysed with phase-resolving modelling approaches, in a depth-integrated manner or with a multi-layer approach, because these approaches can simulate swash motions at the beach face and hence resolve both the wave setup and wave runup (*e.g.,* see Gomes et al., 2016; Nicolae-Lerma et al., 2017; Fiedler et al., 2018; de Beer et al., 2021). However, such modelling approaches remain computationally expensive (several orders of magnitude increase compared to phase-averaged models over a similar domain) and are most often unsuitable for operational purposes or early warning systems at regional and national scales. In this context, it it critical to better understand the impact of the modelling strategy (*e.g.,* resolving depth or not, which formalism for representing the effect of waves on currents) on the accuracy of 3D hydrostatic ocean modelling systems to reproduce the time-averaged wave-induced circulation in the nearshore region. Here, the dynamics of the wave-induced nearshore circulation (mean currents and wave setup) are analysed using a combination of field datasets collected

at Duck, N.C., during two major field campaigns (Duck94 and SandyDuck) and numerical experiments with SCHISM, a 3D unstructured-based hydrostatic ocean modelling system (Zhang et al., 2016). The two storm events from the Duck94 and SandyDuck campaigns considered here are first described in Section 2. Section 3 provides a brief overview of the modelling system SCHISM (Zhang et al., 2016), along with a more detailed description of the recent developments for the parametrisation of various physical processes (*e.g.* the wave-induced vertical mixing). In Section 4, the ability of SCHISM to simulate the cross-shore transformation of directionally-spread irregular waves and the associated depth-varying circulation in the surf zone is assessed, for the first time at such level of details, using the Duck94 dataset that comprises highly-resolved profiles of mean currents along the vertical (Garcez Faria et al., 1998, 2000). The wave setup dynamics are then analysed in Section 5 using the data collected during SandyDuck (Raubenheimer et al., 2001; Apotsos et al., 2007). The ability of the modelling system to simulate the cross-shore distribution of wave setup across the surf zone is first assessed in Section 5.1. The contributions to the simulated wave setup from the different terms of the cross-shore momentum equations are then analysed in Section 5.2 with the objective of quantifying the added-value of using 3D approaches. A particular focus is made at the shoreline, where Apotsos et al. (2007) reported significant underestimations of the wave setup with 2DH radiation stress-based approaches. The main findings are summarised in Section 6, and perspectives for phase-averaged numerical approaches are briefly discussed.

2. Study site and field datasets

The present study uses data collected during storm conditions at the Field Research Facility (FRF), located at Duck, North Carolina (see Fig. 1), during the Duck94 (August to November 1994) and SandyDuck (September to November 1997) series of experiments. During both experiments, comprehensive datasets of surf zone hydrodynamics and sediment transport were collected (Birkemeier et al., 1996) and significantly advanced our understanding of nearshore dynamics. Topographic and bathymetric surveys around the FRF pier have been regularly performed over the last decades using the Coastal Research Amphibious Buggy (CRAB). During major experiments such as Duck94 or SandyDuck, the frequency of these surveys increased and could be performed almost on a daily basis. Wind, atmospheric pressure and mean water level data are continuously collected at the pier while a permanent array of pressure sensors deployed in 8 m-depth continuously provides estimates of the directional wave forcing (hereafter the 8 m array; see Long, 1996, for more details). This monitoring program hence represents a unique opportunity to provide numerical models with accurate and realistic forcing, allowing detailed numerical analyses of the resulting nearshore circulation. The next two sections describe in more details the two storm events considered in the present study, one occurring during Duck94 and the other during SandyDuck.

2.1. Duck94 event (12 October 1994)

The storm event that occurred between 10-13 October during Duck94 was characterized by relatively strong NE winds (Fig. 2b-c), which drove local seas to the field site (typical mean wave period T_{m01} of 6 s, see Fig. 2e). Wind waves initially arrived from the N-NE direction and turned to NE-E towards the 13 October, corresponding to a mean incidence angle decreasing from 12° to 5° (Fig. 2f). Incident waves on the 12 October exhibited a large directional spreading at the 8 m array, as evidenced in Fig. 2g-i. The beach topo-bathymetry was alongshore-uniform during this event (Fig. 1), exhibiting a steep foreshore (1:12), a bar/trough system with the bar crest being located around $x \sim 250$ m, and a much milder slope on the seaward side of the bar (1:170). Note that in this study, all cross-shore (x coordinate) and longshore (y coordinate) positions are provided in the FRF coordinate system. Sediment sampling analyses performed during the experiments revealed that sediments in the surf zone were well-sorted and characterised by a mean grain diameter around 0.2-0.25 mm.

The relatively large wave incident angles combined with the moderately energetic conditions characterising this event (H_{m0} peaked at 2.20 m, see Fig. 2d) generated intense currents, especially around
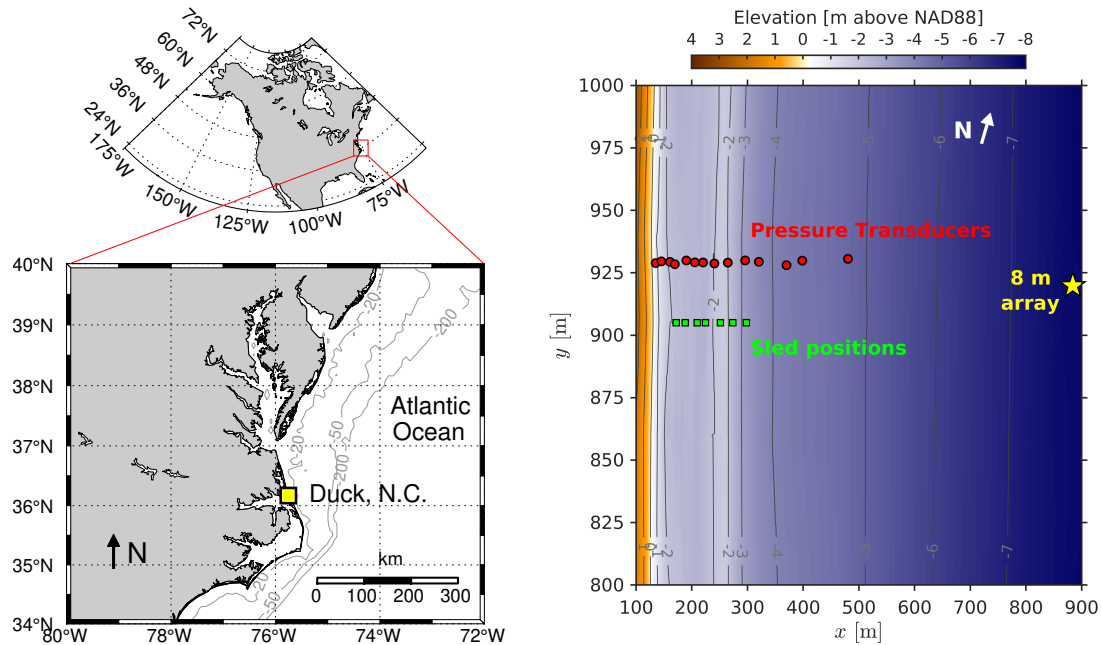
4

Figure 1: The left panel shows a map of the US, zoomed around the field site area of Duck, N.C. (location shown as the yellow square). The coastline around Duck faces the Atlantic Ocean and has a mean orientation of 71.2° with respect to the North. The right panel shows the bathymetry collected on the 12 October during Duck94 in the FRF coordinate system (x : cross-shore coordinate; y : longshore coordinate). The pressure transducers used to verify the wave model predictions across the surf zone were deployed along a cross-shore transect located around $y \sim 930$ m and are shown as red dots (Elgar et al., 1997). The green squares correspond to the seven different positions where the sled structure was deployed on the 12 October ($y \sim 905$ m, Garcez Faria et al., 1998). The yellow star corresponds to the position of the 8 m pressure array, where the offshore wave forcing is estimated (Long, 1996).

147   the sandbar, where the magnitude of longshore currents reached up to 1.0 m/s (Garcez Faria et al., 1998).

148   Detailed measurements of the intensity and vertical distribution of these currents were collected with eight

149   Marsh-McBirney electro-magnetic current meters deployed at fixed heights on a specifically-designed ver-

150   tical structure referred to as the *sled* (see Garcez Faria et al., 1998, 2000, for further details). Assuming no

151   burial of the structure, the current meters were deployed at approximately 23, 42, 68, 101, 147, 179, 224,

152   and 257 cm above the seabed, respectively. The sled was initially towed by the CRAB to the most seaward

153   location for the first run of the experiments. The sled was then pulled by a forklift truck shorewards by

154   10-30 m every hour or so for subsequent runs. A total of seven cross-shore locations were covered on the

155   12 October (see Fig. 1, green squares), corresponding to the measurements runs #1-7 detailed in Table 1

156   and Fig. 2d. Several pressure sensors were also fixed to the sled, providing bulk wave parameters and

157   estimates of the mean sea-surface elevation for each run. The sled dataset is further complemented by

158   bulk wave parameters computed from a series of pressure transducers that collected bottom pressure at

159   2 Hz (see Elgar et al., 1997, for further details). This array of pressure transducers was deployed along a

160   cross-shore transect located slightly North to the sled alongshore positions ($y = 930$, see Fig. 1).

161   The dataset from the 12 October event is now a traditional benchmark for nearshore applications of

162   3D hydrostatic ocean modelling systems (*e.g.*, see Newberger and Allen, 2007b; Uchiyama et al., 2010;

163   Kumar et al., 2012; Moghimi et al., 2013; Zheng et al., 2017). Here, this dataset is principally used to verify

164   the ability of the modelling system SCHISM to represent the 3D wave-induced circulation. A significant

165   novelty compared to previous studies that used such a modelling approach is that all 7 runs from the

166   sled experiments are covered in one single simulation, with time-varying forcing originating from locally-

167   sourced measurements of winds, water levels and directionally-broad waves estimated at the 8 m array.

168   Past modelling studies have only considered monochromatic wave forcing held constant throughout the 7

169   runs, which does not necessarily represent the time-varying incident wave conditions experienced during

170   the storm event. Except for Newberger and Allen (2007b), most past studies have also neglected the effect

171   of tide-induced water level fluctuations, though the mean water depth above the sandbar varied by as
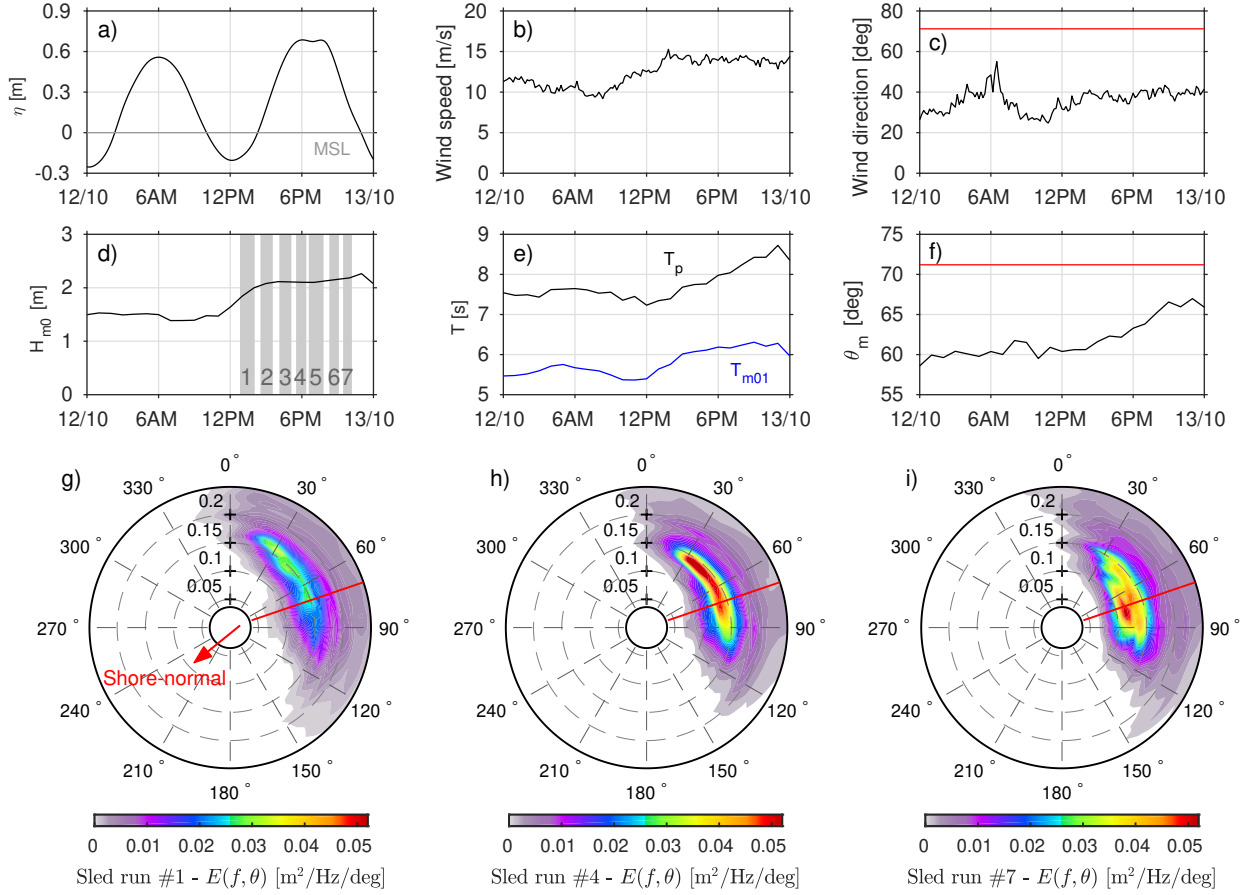
Figure 2: Meteo-oceanographic conditions during the 12 October 1994 storm event. Panels a-b-c show the mean water surface elevation η, the wind speed and direction measured at the FRF pier, respectively. Panels d-e-f show the significant wave height H_{m0}, wave periods (peak T_p and mean T_{m01}) and the mean wave direction θ_m estimated at the 8 m array (meteorological convention). In d), the time and duration of the seven sled runs are indicated with gray shaded areas. Panels g-h-i show the directional wave spectra estimated at the 8 m array at the time corresponding to the sled runs #1, 4 and 7, respectively (see panel d for exact times). Red dashed lines in panels c, f, and g-i indicate the direction corresponding to shore-normal.

Table 1: Details of the sled runs performed on the 12 October 1994. Times are provided relative to Greenwich Mean Time (GMT), which corresponds to local time +5h. The mean water depth at the bar crest ($x \sim 250$ m) is given as an indication of the tidal level (see also Fig. 2a).

Sled runs	#1	#2	#3	#4	#5	#6	#7
Starting time	12:44	14:27	16:02	17:26	18:27	20:13	21:22
Ending time	14:07	15:38	17:13	18:26	19:53	21:10	22:16
x [m]	298	273	252	225	210	188	172
Depth at bar crest [m]	1.96	2.25	2.56	2.70	2.69	2.57	2.24
H_{m0} [m]	1.59	1.61	1.44	1.27	1.12	1.15	1.06
H_{m0} [m] at 8-m array	1.89	2.00	2.05	2.04	2.03	2.09	2.10
T_{m01} [s]	6.14	6.28	6.44	6.29	6.36	6.42	6.38
T_{m01} [s] at 8-m array	6.39	6.67	6.71	6.83	6.85	7.06	7.02

much as 0.8 m throughout the entire sled experiments. By doing so, we aim to evaluate the capacity of SCHISM to reproduce the surf zone circulation in the most detailed and realistic situation as possible since this is then extremely relevant for nearshore applications of this model at regional and national scales (Guérin et al., 2018; Pezerat et al., 2021, 2022; Lavaud et al., 2020, 2022).

2.2. SandyDuck event (13-14 November 1997)

During SandyDuck, field measurements of wave setup were collected at an unprecedented level of accuracy (Raubenheimer et al., 2001; Apotsos et al., 2007), making it a great opportunity to analyse the wave setup dynamics with different modelling strategies (*e.g.*, 2D/3D approaches). The event of interest

occurred around the 13-14 November, when energetic waves drove a relatively large wave setup across the surf zone (up to 0.4 m measured near the shoreline during low-tide on 14/11/1997 6AM). This event was chosen because it is particularly representative of the whole dataset of Apotsos et al. (2007), in which 2DH-based modelling approaches largely underestimate the wave setup close to the shoreline. In more details, the significant wave heights measured during this particular event nearly reached 3 m in 8 m-depth close to high-tide at midnight on the 14 November (Fig. 3b). As the storm initially approached on the 13 November, wind waves predominantly came from the NE direction and were characterised by a peak period of 6-7 s. On the 14th, the peak period increased up to 10 s and waves were mostly normally-incident with respect to the coast. Compared to the Duck94 event introduced above, the beach profile on the 13 November 1997 had a slightly milder foreshore (1:14). A double bar system was evident, with a gently-sloping offshore sandbar located around $x \sim 310$ m, and a steeper sandbar directly connected to the beach face.

The experimental setup for this event is presented in Fig. 3a and is mainly comprised of buried and unburied pressure transducers deployed across the beach at $y \sim 830$ m. The collection and processing of this dataset is fully described in Raubenheimer et al. (2001) so that only the information relevant for this study is provided here. Unburied sensors provided intermittent estimates of the evolution of bulk wave parameters (mostly H_{m0}, see data from p72 in Fig. 3b), which are used to tune the wave breaking parametrisation in the wave model. Altimeters collocated to these unburied pressure transducers continuously measured the elevation of the seabed. The data from these altimeters validated the bathymetric profiles measured by the CRAB on the 11th, which were used to construct the bathymetry. Except for the most landward sensor (circle filled in gray in Fig. 3a), all buried sensors were used to estimate the wave setup (Raubenheimer et al., 2001; Apotsos et al., 2007). The wave setup was estimated as the difference in the mean water surface elevation relative to q39 ($x \sim 445$ m). Thus, this estimate is not absolute as it neglects a few mm or even cm of setdown/setup that can develop seaward of q39 due to shoaling or breaking processes under certain wave conditions.
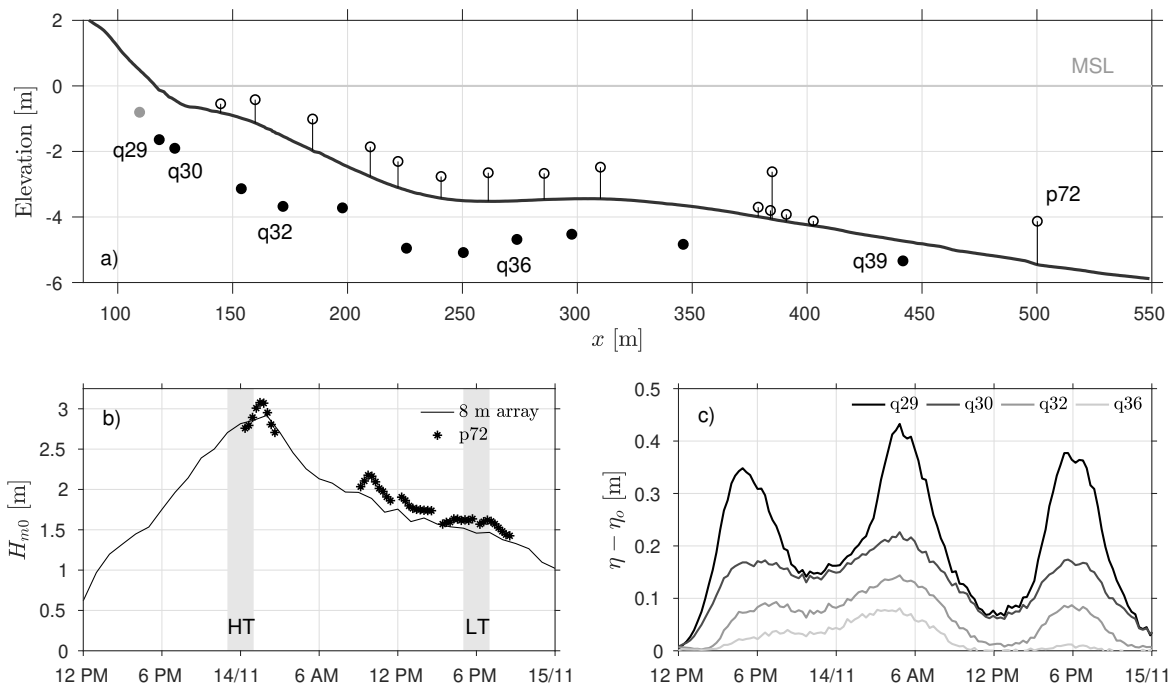

Figure 3: Experimental setup during the 13-14 November storm event (SandyDuck). Panel a) shows the cross-shore location of buried (filled circles) and unburied (open circles) pressure transducers (cross-shore transect located around $y \sim 830$ m). Altimeters were collocated to unburied sensors in order to monitor the evolution of the seabed elevation. Panel b) shows the timeseries of significant wave height H_{m0} during the event measured at the 8 m array (corrected for low bias) and at the most offshore pressure transducers (p72). The two periods of interest are highlighted as gray-shaded areas (high-tide: HT; low-tide: LT). Panel c) shows the time evolution of wave setup relative to q39, estimated at four locations across the surf zone.

Timeseries of wave setup estimated at four locations across the surf zone are shown in Fig. 3c. The wave setup measured during the SandyDuck storm event displays a strong tidal modulation, with the highest values observed at low tides. This is partly explained by the double bar system, with the second bar (see around $x = 125 - 160$ m, Fig. 3a) acting like a narrow terrace, promoting more intense wave energy dissipation over this shallow region at low tide. At the most onshore sensor (q29), the estimated wave setup is well over 0.30 m at low tides, which corresponds to the data points where predictions based on simple cross-shore momemtum balances (*e.g.* Eq. 1) strongly underestimate the wave setup (Raubenheimer et al., 2001; Apotsos et al., 2007). Since wave heights across the surf zone are not available during the first low-tide of 14 November 1997, Section 5 will investigate the wave setup dynamics during SandyDuck by comparing the high-tide situation around midnight on 14 November (HT in Fig. 3b) with the low-tide around 6PM (LT in Fig. 3b).

The initial assessments of the model at the most seaward pressure sensor (p72) revealed a low bias in the modelled significant wave height (of the order of $\sim 10\%$), owing to a low bias in incident wave energy in the directional wave spectra estimated at the 8 m array. The fact that most past studies investigating the wave setup dynamics during SandyDuck used forcing from p72 instead likely explains why this issue has not been reported (at least to the best of our knowledge). Potential explanations for this low bias lie in the method used for reconstructing the directional wave spectra at the 8 m array during storms (Long, 1996). For instance, this approach assumes a flat bottom (*i.e.,* shoaling is neglected between pairs of pressure sensors forming the array), which can be quite a strong hypothesis given that the array spans nearly 175 m in the cross-shore direction, and it uses linear wave theory to convert pressure signals to sea-surface elevation signals, which has also shown limitations for nonlinear waves shoaling in intermediate water depths (*e.g.,* see Martins et al., 2021). Considering the importance of the wave forcing for analysing the different contributions to the wave setup at the shoreline, a correction was directly applied to the measured directional spectra in the form of a constant multiplier to the estimated energy density, in order to remove the low bias at p72.

3. The modelling system: SCHISM

3.1. General description

The transformation of nearshore waves and the resulting hydrodynamic circulation are simulated with SCHISM (Semi-implicit Cross-scale Hydroscience Integrated System Model), a 3D unstructured-grid modelling system (Zhang et al., 2016). The wave effects on currents are represented with the VF formalism described by Bennis et al. (2011) (based on the work of Ardhuin et al., 2008), whose implementation in SCHISM is described in Guérin et al. (2018). The VF framework considers the quasi-Eulerian velocities $(\hat{\mathbf{u}}, \hat{w})$, which are related to the Lagrangian $(\mathbf{u}^l, w^l)$ and Stokes drift $(\mathbf{u}^{st}, w^{st})$ velocities through $(\hat{\mathbf{u}}, \hat{w}) = (\mathbf{u}^l, w^l) - (\mathbf{u}^{st}, w^{st})$. In contrast, when radiation stresses are used instead of the VF for representing the wave effects on currents, the Lagrangian velocities are solved and the reader is referred to Roland et al. (2012) for their implementation in SCHISM.

SCHISM solves the 3D Reynolds-averaged Navier-Stokes equations with the assumption that the pressure is hydrostatic (Zhang and Baptista, 2008; Zhang et al., 2016). Conservation of mass is ensured via the resolution of the following continuity equations (in 3D and depth-averaged form respectively) for the quasi-Eulerian velocities $(\hat{\mathbf{u}}, \hat{w})$ and the free surface elevation η:

$$\nabla \cdot \hat{\mathbf{u}} + \frac{\partial \hat{w}}{\partial z} = 0 \tag{2}$$

$$\frac{\partial \eta}{\partial t} + \nabla \cdot \int_{z_b}^{\eta} \left(\hat{\mathbf{u}} + \mathbf{u}^{st} \right) dz = 0 \tag{3}$$

The momentum equation, resolved at each vertical layer, reads:

$$\frac{D\hat{\mathbf{u}}}{Dt} = \frac{\partial}{\partial z}\left(v\frac{\partial \hat{\mathbf{u}}}{\partial z}\right) - g\nabla\eta + \mathbf{F} \tag{4}$$

where:

∇	Nabla operator: $(\frac{\partial}{\partial x}, \frac{\partial}{\partial y})$
D/Dt	material derivative
(x, y)	horizontal Cartesian coordinates
z	vertical coordinates, positive upward
z_b	seabed elevation
t	time
η	mean free surface elevation
$\hat{\mathbf{u}}$	quasi-Eulerian horizontal velocity vector, with Cartesian components: $\hat{\mathbf{u}} = (\hat{u}, \hat{v})$
$\hat{w}$	quasi-Eulerian vertical velocity
v	vertical eddy viscosity [m^2.s^{-1}]
g	acceleration of gravity [m.s^{-2}]
$\mathbf{F}$	forcing terms [m.s^{-2}]: wave forces, baroclinic gradient, horizontal viscosity, Coriolis, earth tidal potential and atmospheric pressure

A key feature of SCHISM is the treatment of the advection term in Eq. 4 by an Eulerian-Lagrangian method, which relaxes the numerical stability constraints of the model (Zhang et al., 2016). The hydrodynamic solver of SCHISM requires Courant-Friedrichs-Lewy (CFL) numbers greater than 0.4 which, with a spatial resolution of O(m), allows for timesteps of O(s) in surf zone applications. The wind forcing enters as a boundary condition at the sea surface, where SCHISM enforces a balance between the internal Reynolds stress and the applied wind shear stress (Zhang and Baptista, 2008). At the bottom, the frictional shear stress $\boldsymbol{\tau_b}$ is represented with the following classic form:

$$\boldsymbol{\tau_b} = C_D|\hat{\mathbf{u}}_b|\hat{\mathbf{u}}_b \tag{5}$$

where C_D is the bottom drag coefficient (Blumberg and Mellor, 1987) and $\hat{\mathbf{u}}_b$ is the quasi-Eulerian horizontal velocity vector at the top of the bottom cell. In practice, the bottom shear stresses intervene in the balance with the internal Reynolds stresses inside the turbulent boundary layer (Zhang et al., 2016). In a typical surf zone situation, where both $\hat{\mathbf{u}}_b$ and the depth-averaged current velocity vector $\hat{\mathbf{U}}$ are seaward-oriented (*e.g.*, see Pezerat et al., 2022), the VF formalism will hence naturally account for the contribution from the cross-shore component of $\boldsymbol{\tau_b}$ to the wave setup. This contrasts with the radiation stress formalism, where the cross-shore Lagrangian depth-integrated velocity is null. As a consequence, the bottom shear stress contribution to the wave setup is not naturally incorporated with the radiation stress formalism.

Given the spatial scale of our nearshore application ($\sim$ 1 km-long in the cross-shore direction, up to 8 m depth) and the absence of estuaries, we here neglect baroclinic forces. Similarly, horizontal viscosity, the earth tidal potential and atmospheric pressure are not applied here (the latter two being unneeded since we use locally-sourced water levels that already incorporate surges). In the nearshore region, the contribution from surface gravity waves to $\mathbf{F}$ - here denoted $\mathbf{F}^{\text{w}} = (F_x^{\text{w}}, F_y^{\text{w}})$ - is the dominant term. With the VF formalism, the two components of the wave forces F_x^{w} and F_y^{w} can be decomposed into conservative (adiabatic) and non-conservative (dissipative) components as follows (Bennis et al., 2011):

$$F_x^{\text{w}} = v^{\text{st}}\left[f_C + \left(\frac{\partial \hat{v}}{\partial x} - \frac{\partial \hat{u}}{\partial y}\right)\right] - w^{\text{st}}\frac{\partial \hat{u}}{\partial z} - \frac{\partial J}{\partial x} + F_x^{\text{br}} + F_x^{\text{fr}} \tag{6}$$

$$F_y^{\text{w}} = -u^{\text{st}}\left[f_C + \left(\frac{\partial \hat{v}}{\partial x} - \frac{\partial \hat{u}}{\partial y}\right)\right] - w^{\text{st}}\frac{\partial \hat{v}}{\partial z} - \frac{\partial J}{\partial y} + F_y^{\text{br}} + F_y^{\text{fr}} \tag{7}$$

where f_C is the Coriolis parameter, J is the wave-induced mean pressure, $\mathbf{F}^{br}$ is the non-conservative forces due to depth-induced wave breaking (Bennis et al., 2011; Guérin et al., 2018) while $\mathbf{F}^{fr}$ is the bottom streaming represented with the approach of Uchiyama et al. (2010). The expressions for all conservative terms of the wave forces are recalled in Appendix A.

3.2. Spectral wave modelling

The wave forces (Eq. 6 and 7) are computed within WWM-II, a third-generation spectral wave model that simulates the generation, propagation and transformation of short waves (Roland et al., 2012). The wave model is fully-coupled to the hydrodynamic core of SCHISM at the code level, and both models share the same unstructured grid and domain decomposition, avoiding interpolation errors during the exchange of variables (mainly η, $\hat{\mathbf{u}}$, $\hat{w}$, $\mathbf{u}^{st}$, w^{st} and $\mathbf{F}^{w}$).

WWM-II solves the following equation for the conservation of the wave action $N(\sigma, \theta)$ (e.g., see Komen et al., 1994):

$$\frac{\partial N}{\partial t} + \nabla \cdot (\mathbf{c_g} + \hat{\mathbf{U}}) N + \frac{\partial}{\partial \sigma}(c_\sigma N) + \frac{\partial}{\partial \theta}(c_\theta N) = \frac{S}{\sigma} \tag{8}$$

where:

σ relative wave frequency ($\sigma = 2\pi f$, with f the wave frequency)

θ wave direction

$\mathbf{c_g}$ wave group velocity vector; $\mathbf{c_g} = c_g (\cos\theta, \sin\theta)$ where c_g is the wave group velocity taken from linear wave theory

c_σ advection speed in the σ-space

c_θ advection speed in the θ-space

N wave action density spectrum, related to the wave energy density spectrum E by $N = E/\sigma$

$\hat{\mathbf{U}}$ depth-integrated quasi-Eulerian horizontal velocity vector ($\hat{\mathbf{U}} = (\hat{U}, \hat{V})$)

S source terms

S incorporates source and sink terms that affect waves at every stage of their propagation (Roland et al., 2012). Though the spatial scale of our application is small (~ 1 km-long in the cross-shore direction), the energy input from the wind S_{in} is modelled with the parameterizations of Ardhuin et al. (2010). The source term for whitecapping S_{wc}, and its related contribution to the vertical mixing are neglected here since the dissipation mainly occurs through depth-induced breaking. Non-linear interactions between quadruplets (S_{nl4}) are modelled following Hasselmann et al. (1985) while the approach of Eldeberky (1996) is used to estimate non-linear interactions between triads of frequencies (S_{nl3}). The energy dissipation via bottom friction is modelled with the SHOWEX parameterization (Ardhuin et al., 2003) using mean grain diameters estimated during the field campaigns. The parameterization for the depth-induced wave breaking source term S_{br} is described next, along with the surface roller model recently implemented in SCHISM.

3.3. Depth-induced wave breaking and surface roller model

The formulation of van der Westhuysen (2010) is used to model the wave breaking-induced energy dissipation ϵ_w. This parameterization is based on a phase-averaged approximation of the biphase $\mathcal{B}_p$ of self-interacting components at the peak frequency (Eldeberky, 1996) and reads:

$$\epsilon_w = \frac{3}{16\sqrt{\pi}} \rho g \overline{f} B \left(\frac{\mathcal{B}_p}{\mathcal{B}_{ref}}\right)^n \frac{H_{rms}^3}{h}, \tag{9}$$

where $\overline{f}$ is the mean centroid frequency ($\overline{f} = 1/T_{m01}$), B is a breaking coefficient, $\mathcal{B}_{ref}$ is the biphase at which all waves are considered broken and H_{rms} is the root-mean square wave height computed from the significant wave height H_{m0} as $H_{m0}/\sqrt{2}$ (van der Westhuysen, 2010). After some calibration against field data, the breaking criterion $\mathcal{B}_{ref}$ was set to -1.25 (default is $-4\pi/9 = -1.39$) while the value of $n = 2.5$ as proposed by van der Westhuysen (2010) was retained. The beach slope-dependent parameterization for

the breaking coefficient B introduced by Pezerat et al. (2021) is used in order to better reproduce the incident wave transformation on the seaward side of the sandbar system at Duck. In the absence of knowledge on the frequency-dependence of the energy dissipation by breaking, ϵ_w is spread in frequencies and directions in proportion of the corresponding energy in order to define the source term S_{br}, following Eldeberky and Battjes (1996).

The rate of wave energy dissipation during breaking ϵ_w directly controls the growth of surface rollers, which are turbulent masses of mixed air and water advected by breaking waves that contribute to the mean circulation of the surf zone (Svendsen, 1984b; Deigaard et al., 1991; Stive and de Vriend, 1994). The evolution of surface rollers bulk energy E_r is here modelled following Reniers et al. (2004):

$$\frac{\partial E_r}{\partial t} + 2\nabla \cdot (\mathbf{c_p} + \hat{\mathbf{U}})E_r = \alpha_r \epsilon_w - \epsilon_r, \tag{10}$$

where $\mathbf{c_p}$ is the wave phase velocity vector corresponding to the (continuous) peak frequency ($\mathbf{c_p} = c_p(\cos\theta_m, \sin\theta_m)$ in which c_p is determined from the linear wave dispersion relation and θ_m corresponds to the mean wave direction), $\alpha_r \in [0,1]$ is a parameter controlling the efficiency of energy transfers from breaking waves to rollers and ϵ_r is the rate of energy dissipated through shear stresses at the wave/roller inner interface (*e.g.*, see Duncan, 1981; Deigaard and Fredsøe, 1989). Surface rollers also dissipate some energy through mass exchanges at the wave/roller interface (see Appendix by R. Deigaard in Stive and de Vriend, 1994), which explains the factor 2 in the advection term. The dissipation term ϵ_r can be expressed as a function of both wave and roller properties (*e.g.* roller length or area, see Duncan, 1981; Svendsen, 1984b; Deigaard et al., 1991), however, significant uncertainties exist regarding the roller area formulations and the void ratio in rollers (Martins et al., 2018). More conveniently, ϵ_r is directly written as a function of the roller energy E_r and the angle β_r at the wave/roller inner interface, following Reniers et al. (2004):

$$\epsilon_r = \frac{2g\sin\beta_r}{c_p}E_r \tag{11}$$

The contribution M_r from surface rollers to the total mass flux is simply related to the roller energy as $M_r = 2E_r/c_p$ (*e.g.*, see Reniers et al., 2004). Although in theory this transport primarily occurs near the surface, above through level, there is no consensus on its vertical distribution. We here choose to apply the roller contribution to the total Stokes drift velocities $\mathbf{u}_r^{st} = M_r(\cos\theta_m, \sin\theta_m)/\rho h$, with ρ the mean water density, in a depth-uniform manner.

The present roller model only has two parameters: α_r, which controls the growth of the surface roller, and $\sin\beta_r$, which controls the energy dissipation rate in the roller. Similar to most studies using fully coupled 3D wave-current interaction models, $\alpha_r = 1$ (*i.e.* full conversion) is the present choice since it provided the most accurate results when assessed against field data. We can note, however, that lower values have been used in models that included non-linear wave effects in the surf zone (*e.g.*, $\alpha_r = 0.65$ taken in Michallet et al., 2011). Similarly, the common value of 0.1 for $\sin\beta_r$ is also retained here. This corresponds to mean angles of the wave/roller inner interface $\beta_r \sim 5.7°$. This value might appear small but it should be stressed that β_r refers to the roller inner interface, and not the surface roller angles at the air/roller, which can be much higher (by up to a factor 4, *e.g.*, see Martins et al., 2018).

Eq. 10 is solved explicitly in time with a slightly different numerical approach than that described in Roland et al. (2012). The geographical advection is performed with the N-scheme, which belongs to the Residual-Distribution framework described in Abgrall (2006). No time splitting is performed and the source terms (right-hand side of Eq. 10) are directly integrated during the sub-iterations of the advection, following Deconinck and Ricchiuto (2007, their Eq. 27). Besides the fact that this integration method is relatively simple to implement, it has two main advantages: 1) there are no splitting errors associated with this approach and, 2) since the local timestep is dictated by the advection, the CFL condition related to the integration of source terms (*e.g.*, see Hargreaves and Annan, 2001) is always naturally fulfilled, which

makes the integration process accurate and stable.

348   The expression for the source of quasi-Eulerian momentum due to depth-induced wave breaking is
349 directly defined from ϵ_w and ϵ_r as follows:

$$\mathbf{F}^{\mathrm{br}} = f_{br}(z)\frac{\epsilon_r}{\rho c_p}(\cos\theta_m, \sin\theta_m) - f_{br}(z)\frac{g}{\rho}\int_0^{2\pi}\int_0^{\infty}(1 - \alpha_R)\frac{S_{br}}{\sigma}\mathbf{k}\,d\sigma d\theta \tag{12}$$

350 where $f_{br}(z)$ is an empirical function distributing the momentum related to wave breaking along the
351 vertical. In the present study, the forcing is applied as a surface shear stress (Deigaard, 1993), *i.e.* with
352 $f_{br} = 1$ in the upper layer and 0 elsewhere. In the radiation stress formalism, the contribution from surface
353 rollers was represented following the approach of Apotsos et al. (2007).

3.4. Vertical mixing and wave-enhanced turbulence

355   Breaking waves produce significant quantities of turbulent kinetic energy $\mathcal{K}$ at the sea surface, which
356 can then penetrate deep into the water column (*e.g.*, see Stive and Wind, 1982; Ting and Kirby, 1995;
357 Terray et al., 1996). Accounting for this source of turbulent kinetic energy at the surface is critical for
358 accurately modelling the vertical mixing, which controls the vertical shear of currents in the nearshore
359 region. One-dimensional (vertical) turbulence closure models have been successfully applied to represent
360 the effects of wave breaking on the vertical mixing (Craig and Banner, 1994; Burchard, 2001; Feddersen and
361 Trowbridge, 2005) so that their use in 3D nearshore hydrodynamic models is now widespread (Newberger
362 and Allen, 2007b; Kumar et al., 2012; Moghimi et al., 2013, 2016; Delpey et al., 2014). Here, we use a
363 similar approach as that of Moghimi et al. (2016) to simulate the production and decay of $\mathcal{K}$ across the
364 water column. This approach relies on the generic length scale (GLS) two-equation turbulence closure
365 model of Umlauf and Burchard (2003), implemented within the General Ocean Turbulence Model (GOTM)
366 coupled with SCHISM. The choice of model parameters is made so that the $\mathcal{K}$-ω model of Wilcox (1988)
367 is recovered, where ω is the specific dissipation rate, related to $\mathcal{K}$ and the turbulence dissipation rate
368 ϵ_{tke} by $\omega = \epsilon_{tke}/(0.3^2\mathcal{K})$. The eddy viscosity ν, which controls the vertical mixing in the hydrodynamics
369 module (see Eq. 4), is then computed as $\nu = (0.3\mathcal{K})^{1/2}l$, where l is the turbulence mixing length defined as
370 $l = (0.3\mathcal{K})^{3/2}/\epsilon_{tke}$.

371   The production of turbulent kinetic energy by breaking waves is modelled through a flux-type boundary
372 condition at the surface, following Feddersen and Trowbridge (2005):

$$\frac{\nu}{\sigma_{\mathcal{K}}}\frac{\partial\mathcal{K}}{\partial z} = F_{tke}\left(\frac{z_0^s - z^{\mathrm{t}}}{z_0^s}\right)^{\frac{3}{2}\alpha} \quad \text{at } z = \eta \tag{13}$$

373 where F_{tke} (in m^3/s^3) is the turbulent kinetic energy injected at the sea surface, $\sigma_{\mathcal{K}}$ is the turbulent Schmidt
374 number ($\sigma_{\mathcal{K}} = 2$ for the $\mathcal{K}$-ω model), $\alpha = -2.53$ is the partial decay rate of $\mathcal{K}$ in the wave enhanced layer,
375 z_0^s is the surface roughness length and z^{t} is the elevation corresponding to the middle of the top cell (where
376 the flux is actually applied). The flux of turbulent kinetic energy injected at the surface is dictated by the
377 intensity of wave breaking processes through $F_{tke} = c_{br}\left[\epsilon_w + \epsilon_r\right]/\rho$, where c_{br} is a coefficient controlling
378 the amount of energy to be injected (ranging between 0.01-0.25, *e.g.*, see Feddersen and Trowbridge, 2005;
379 Huang et al., 2009; Feddersen, 2012). Note that other authors use a factor $(1 - \alpha_r)$ before ϵ_w, while we
380 here consider that both breaking waves and rollers contribute to $\mathcal{K}$ injection at the surface. The vertical
381 distribution of turbulent kinetic energy in the upper portion of the water column strongly varies with the
382 surface roughness length z_0^s. Although some dependency on the type of breakers or with the primary
383 wavelength are expected, the parameterisation of z_0^s remains poorly understood due to the difficulties in
384 measuring this quantity. Adopting the deep water parameterisation of Terray et al. (1996) to the nearshore
385 area, it is generally expressed as a function of the significant wave height: $z_0^s = \alpha_w H_{m0}$, with $\alpha_w = O(1)$
386 (Moghimi et al., 2016). Other studies take this parameter constant, *e.g.*, $z_0^s = 0.1$ m in Craig and Banner

387 (1994) or $z_0^s = 0.2$ m in Feddersen and Trowbridge (2005). The influence of the choice of z_0^s on the vertical
388 variation of $\hat{\mathbf{u}}$ will be analysed in Section 4.2.

3.5. Model implementation

390   The seaward extent of the model was taken at the cross-shore location corresponding to the 8-m pressure
391 array ($x \sim 870$ m in the FRF reference system, see Figure 1). The horizontal resolution of the unstructured
392 computational grid is constant over the upper beach region (resolution of 3 m up to $x \sim 145$ m), and then
393 decreases almost linearly in the cross-shore direction to reach 35 m at the offshore limit. The vertical is
394 discretized with 30 S-levels, with increased resolution at the surface and near the bottom (*e.g.*, bottom
395 and top layer thickness of 0.005 m at the bar crest). This choice is typical for nearshore applications of
396 3D hydrostatic ocean modelling systems, providing a good balance between computational efficiency and
397 accurate reproduction of the breaking wave-induced turbulent kinetic energy near the surface. For both
398 events considered here, the topo-bathymetric data collected with the CRAB on the same day (Duck94)
399 or a few days earlier (SandyDuck) were linearly interpolated on the computational grid (no smoothing
400 used). Note that we systematically use Mean Sea Level (MSL) as vertical datum, which corresponds to
401 North American Vertical Datum of 1988 (NAVD88) minus 0.128 m at Duck. The wave effects on the bottom
402 shear stress is modelled following Soulsby (2005), with a bottom roughness length of 0.001 m, which
403 corresponds to the best-fit results of Uchiyama et al. (2010). In the following, the importance of resolving
404 the depth-varying surf zone circulation in wave setup predictions is assessed by comparing 2DH and 3D
405 simulations. To ensure a consistent comparisons between such model configurations in terms of bottom
406 drag coefficient C_D, we follow the approach of Zheng et al. (2013), which uses the relation between the
407 Manning coefficient n in 2DH with the bottom roughness z_0 taken in 3D (Bretschneider et al., 1986).

408   The offshore wave forcing corresponds to hourly wave directional spectra estimated from the 15
409 pressure gauges that constitute the 8 m array (see Fig. 1 for the location and Long, 1996, for more details).
410 At the offshore boundary, we also impose the water levels measured at the pier by the NOAA tidal station
411 every 6 minutes. As winds are measured at a height of 18.8 m above the pier, wind speeds at 10 m were
412 obtained assuming a logarithm vertical profile and a sea surface roughness of $z_{0,w} = 0.0095$ m (obtained
413 by WWM-II), and were taken constant over the whole domain. Periodic type of boundary conditions are
414 applied at the lateral boundaries (North and South of the field site) for both wave and hydrodynamic
415 modules, which is essential for accurately reproducing the cross-shore distribution of longshore currents
416 along this relatively straight and uninterrupted coastline. Finally, the time step for the circulation model
417 is set to 2 s whereas WWM-II runs in implicit mode with a time step of 10 s (Roland, 2009). The spectral
418 space used 24 frequencies ranging from 0.05 to 0.45 Hz while a resolution of 2.5° was used to discretize the
419 directions that spanned from 345° to 135°.

4. Assessment of the modelling system during Duck94

421   This Section aims at assessing the ability of the modelling system SCHISM in its *baseline* configuration
422 (3D-VF) to simulate the transformation of directionally-broad short waves across the surf zone and the
423 associated water levels and depth-varying mean currents. The dataset collected on the 12 October 1994
424 during Duck94 and presented in Section 2.1 is used for this purpose. The cross-shore transformation of
425 incident waves and the contribution of surface rollers are first examined in Section 4.1. The depth-varying
426 circulation and its sensitivity to the vertical mixing parametrisation are then addressed in Section 4.2.

4.1. Wave transformation and depth-averaged circulation

428   Fig. 4d shows, at the time corresponding to sled run #3, that WWM-II accurately predicts the cross-
429 shore transformation of incident waves. The rapid decrease of significant wave height H_{m0} landward
430 of $x \sim 290$ m suggests that the dissipation of incident wave energy principally occurs via depth-induced
431 breaking over the prominent sandbar located around $x \sim 250$ m (Fig. 4a and 4c). Normalised root-mean

square discrepancies (NRMSD) for H_{m0} during this specific sled run are around 6% (see Table 2). NRMSDs for all sled runs are between 6 and 10%, which confirms that the model also captures well the transition from a low- (run #1) to high-tide situation (runs #4 and #5). Excluding the first two sensors from this computation leads to NRMSD < 4% for most runs. The experimental dataset used for this assessment was collected along the $y = 930$ m transect (Elgar et al., 1997), which is located approximately 25 m northwards of that where the sled experiment took place (Fig. 1). While the beach profile was mostly alongshore-uniform on the 12 October (see Fig. 1), the upper section of the beach did exhibit some alongshore variability, with the beach face at $y = 930$ m being located slightly more landwards. This explains, at least in part, the slight over-dissipation of incident wave energy observed around $x \sim 135$ m (Fig. 4d).

While depth-induced breaking ceases rapidly once incident waves transition to the trough (see the abrupt decrease of ϵ_w/ρ starting around $x \sim 250$ m in Fig. 4c), surface rollers gradually dissipate the energy gained over the sandbar. This process is partly responsible for the shoreward translation of the depth-integrated alongshore current peak and the enhanced current magnitude over the trough region (Fig. 4f). As discussed by Uchiyama et al. (2010), the vertically-varying VF also contributes to the landward shift of maximal longshore velocity near the bar crest (compare 2DH and 3D simulations without rollers in Fig. 4f). By shifting landwards wave breaking-induced forces, surface rollers also affect the cross-shore distribution of wave setup by translating shorewards the point where the barotropic gradient ($\partial\eta/\partial x$) is largest in magnitude (Apotsos et al., 2007), and by increasing the setup in the trough region by ~5% (Fig. 4b). From these comparisons, we also note that the predicted wave setup is greater when representing the surf zone depth-varying circulation in both the trough region (by 5-8%) and at the shoreline ($\sim 25\%$ over the 1:12 foreshore), which is consistent with the conclusions from Guérin et al. (2018). This will be further analysed in Section 5 using the SandyDuck dataset. The good match observed along the cross-shore transect between $\widehat{U}$ and $-(U^{st} + U_r^{st})$ (Fig. 4e) suggests that the cross-shore quasi-Eulerian mean current (seaward-oriented return current) compensates for the onshore-directed mass transport associated with incident waves and rollers, which is expected given the near longshore-uniform situation. Surface rollers significantly contribute to the mass transport in the surf zone (up to 25% over the sandbar), as evidenced by the enhanced depth-averaged cross-shore current velocities compared to the simulation without rollers (Fig. 4e).

4.2. Depth-varying surf zone circulation

Fig. 5 presents the vertical distribution of cross-shore (panel a) and longshore (panel b) current velocities during the seven sled runs on 12 October. The *baseline* simulation is compared to a simulation that does not account for the effects of surface rollers in order to further illustrate their contribution to the surf zone

Table 2: Normalized root mean square discrepancy (NRMSD) of significant wave height H_{m0}, mean surface elevation η, cross-shore $\hat{u}$ and longshore $\hat{v}$ velocities modelled during the 12 October sled experiments. The performaces of two simulations are quantified here: the baseline 3D-VF simulation that includes the effects of surface rollers and the 3D-VF simulation without it. The NRMSD (in %) are computed as $100x\left[\sum_{i=1}^{N}(d_i - m_i)^2 / \sum_{i=1}^{N} d_i^2\right]^{1/2}$ where N is the number of sensors, d_i is the datum measured at sensor i while m_i is the modelled one. NRMSD for H_{m0} are computed using the cross-shore array of pressure sensors at $y \sim 940$ (Elgar et al., 1997) at the mean time corresponding to the specific sled run. For the wave setup NRMSD, the error was normalised by the tidal range measured during the experiments (0.8 m).

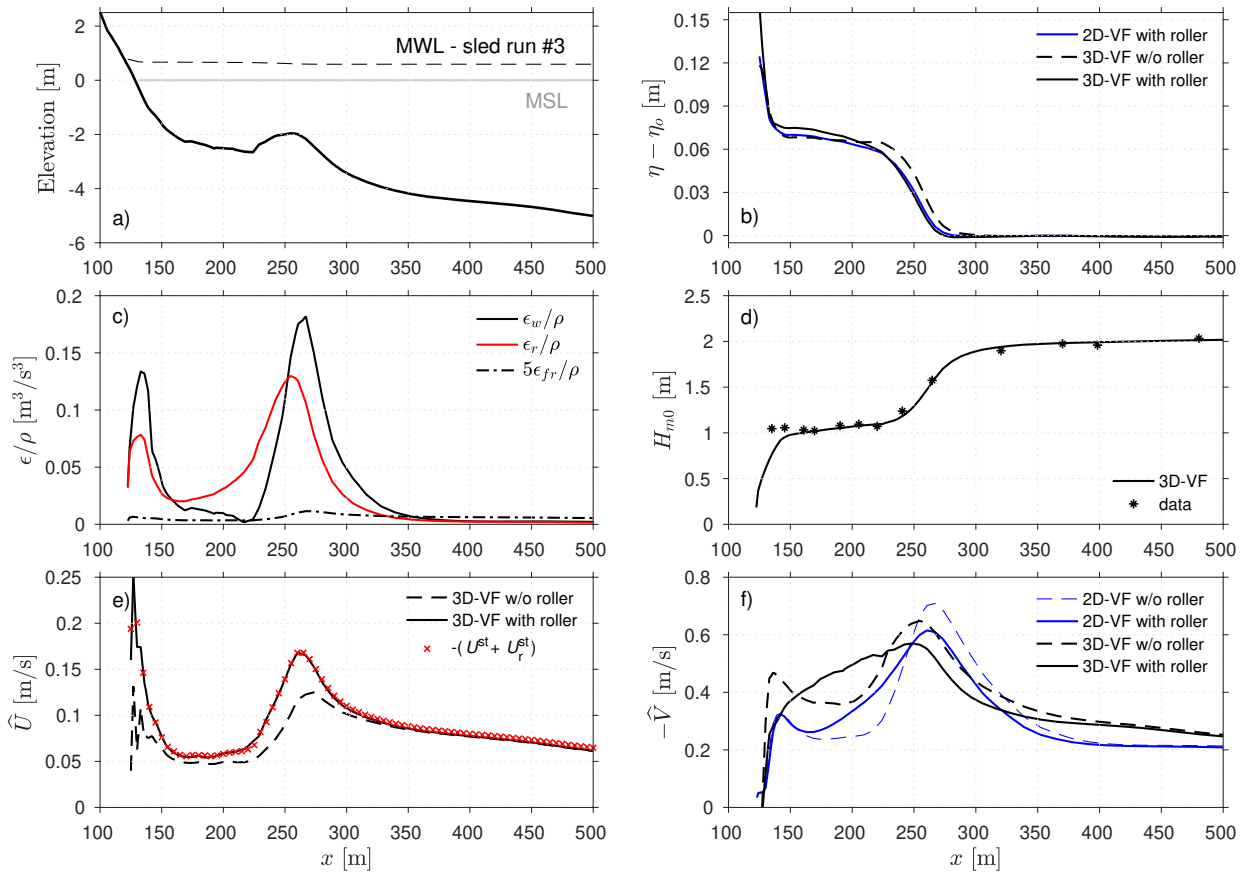| Sled runs		#1	#2	#3	#4	#5	#6	#7
	H_{m0}	10.0	9.0	6.1	6.2	6.7	7.0	7.6
With rollers	η	3.2	4.4	10.7	0.7	12.6	2.5	0.3
	$\hat{u}$	29.2	28.1	16.7	23.5	9.9	35.6	35.0
	$\hat{v}$	5.0	22.0	11.2	26.5	22.5	12.4	12.8
Without rollers	η	3.6	3.2	8.7	1.7	13.0	1.7	2.0
	$\hat{u}$	44.6	38.6	16.6	50.3	47.5	36.6	26.9
	$\hat{v}$	18.9	37.4	18.6	28.3	36.9	18.0	14.8

14

Figure 4: Range of bulk and depth-integrated quantities simulated during sled run #3 of October 12th, DUCK94. Panel a) shows the beach topography relative to Mean Sea Level (MSL). The Mean Water Level (MWL) during run #3 is also shown as black dashed line (mean offshore surface elevation $\eta_o = 0.53$ m). Panel b) compares the wave setup ($\eta - \eta_o$) computed using the 2D radiation stress (2D-RS) formalism or the 3D vortex force formalism (3D-VF), and with or without the effects of surface rollers. The simulated significant wave height H_{m0} are compared with data from Elgar et al. (1997) in panel d) while the associated energy dissipation (divided by ρ) is shown in panel c). Simulated cross-shore and longshore depth-averaged currents are shown in panels e) and f), respectively.

3D circulation. At each cross-shore location corresponding to a sled run, observations represent a 10-min average of current velocities. Overall, the *baseline* simulation demonstrates a fairly good agreement with observations, with NRMSD similar to those obtained in previous studies that used synthetic forcing (see Table 2). Predicted mean surface elevations (Fig. 5b) compare fairly well with estimates derived from a sled-mounted pressure transducer (NRMSD within 12% for each run, see Table 2). Note that these errors include uncertainties on both the seabed elevation and that of the sensor above the seabed, since the sled structure potentially buried by a few cm. The intensity and vertical distribution of longshore currents (Fig. 5b) are well reproduced with NRMSD ranging from 5 to 25%. As in other studies (Newberger and Allen, 2007b; Zheng et al., 2017), the current magnitude is underestimated during runs #4 and 5, which remains unexplained. Representing surface rollers only has a minor effect on the cross-shore distribution of alongshore currents in the trough, however, their magnitude is reduced by as much as 15% on and seaward of the bar crest, leading to a better match with observations (Table 2). The effect of surface rollers on cross-shore current velocities is more pronounced, with enhanced mass transport at the bar crest (run #3 in Fig. 5a), and much more vertically-sheared and intense return currents at the locations corresponding to sled runs #4 and #5 (NRMSD of $\hat{u}$ consistently improved, see Table 2). The latter is explained by the combined effect of more intense forcing applied at the surface when rollers are represented (*e.g.*, see Fig. 4c) and the enhanced mixing at these cross-shore locations (see Fig. 5c-d).

The comparison of cross-shore current velocities $\hat{u}$ with observations shows contrasting characteristics across the monitored beach profile (Fig. 5a). At locations #3 and #5, $\hat{u}$ is very accurately predicted (NRMSD $\lesssim 17\%$), both in terms of vertical distribution (shear) and magnitude. The discrepancies at #4
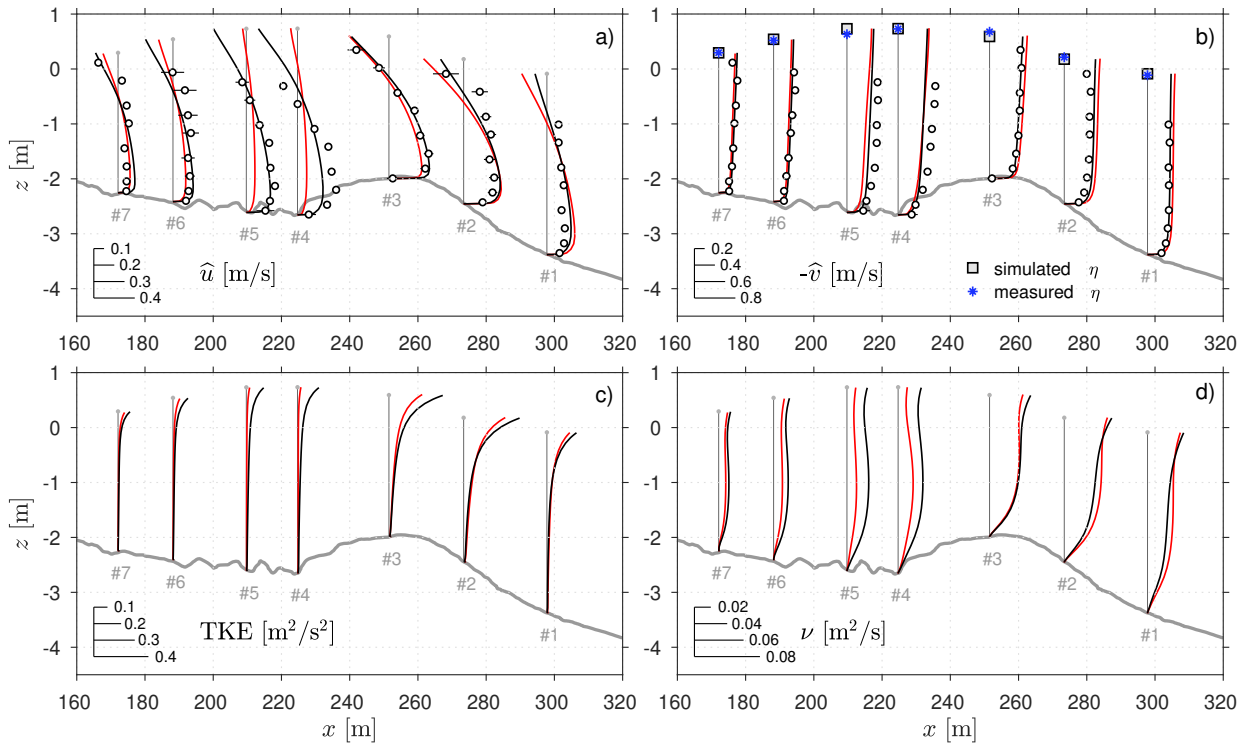
Figure 5: Comparison of modelled cross-shore (a) and longshore (b) current velocities against observations collected on the sled structure, with (black lines) or without (red lines) the effects of surface rollers. $\hat{u}$ and $\hat{v}$ are positive to the East and North, respectively. Error bars on observation data points represent one standard deviation of the 10-min window-averaged current velocities computed over the whole sled run. The simulated mean surface elevations are compared in panel b) with observations derived from a pressure transducer (#22) mounted on the sled structure. Panels c) and d) show the simulated vertical distribution of TKE and eddy viscosity ν, respectively. The cross-shore location of each sled run is shown as the thin vertical line above the corresponding sled run number.

484   are found in most studies employing this dataset and remain, to the best of our knowledge, unexplained.

485   Seaward of the bar crest, a significant amount of incident wave energy is dissipated through depth-induced

486   breaking (Fig. 4c). Despite the strong injection of TKE at #1 and #2 and the associated mixing (Fig. 5c-d),

487   the modelled profiles of $\hat{u}$ appear overly sheared at these locations, leading to an overestimation of the

488   seaward-oriented current near the bottom. A similar observation can be made at #6 and #7 though the

489   wave breaking-induced forcing is weaker in the trough region. Considering the correct representation of

490   longshore currents at these locations, this suggests that the vertical mixing is underestimated in the present

491   modelling approach.

492   Fig. 6 investigates the sensitivity of the model to the choice of the surface mixing length z_0^s at the

493   positions corresponding to run #3 (panels a-d) and #6 (panels e-h). Over the sandbar, the choice of z_0^s has a

494   negligible effect on the intensity of longshore currents $\hat{v}$ (Fig. 6b), whereas in the trough region (Fig. 6f), $\hat{v}$

495   weakens with increasing surface mixing length (Feddersen and Trowbridge, 2005). In contrast, the vertical

496   distribution of $\hat{u}$ appears more sensitive to the choice of z_0^s at both locations. For z_0^s taken constant at 0.2 m

497   (Feddersen and Trowbridge, 2005), the injected TKE does not penetrate deeply into the water column (Fig.

498   6c and 6g), yielding a weak vertical mixing near the surface (an order of magnitude difference compared to

499   $z_0^s = 1.2H_{m0}$, see Fig. 6d and 6h). This results in unrealistically large onshore-directed currents at the surface

500   ($\hat{u} \sim -1.2$ m/s at #3) and overestimated return currents near the bottom (Fig. 6a and 6e). Although at #3,

501   the *baseline* model ($z_0^s = 1.2H_{m0}$) provides the most accurate predictions of $\hat{u}$, the vertical mixing is clearly

502   insufficient for describing the relatively depth-uniform cross-shore velocities at #6, even with the largest

503   values of z_0^s reported in the literature ($z_0^s = 1.5H_{m0}$). The presence of large shear waves on the 12 October

504   possibly contributes to the vertical mixing, a process which is not accounted for in the present modelling

505   approach. Shear waves appear as very-low frequency oscillations in the 10-min averaged current velocity

506   timeseries (see standard deviation in data points, Fig. 6), whose amplitude vary between 0.1 m/s at #1

507   and 0.2 m/s at #6 on this day. These are ubiquitous at the Duck site when energetic waves arrive with a
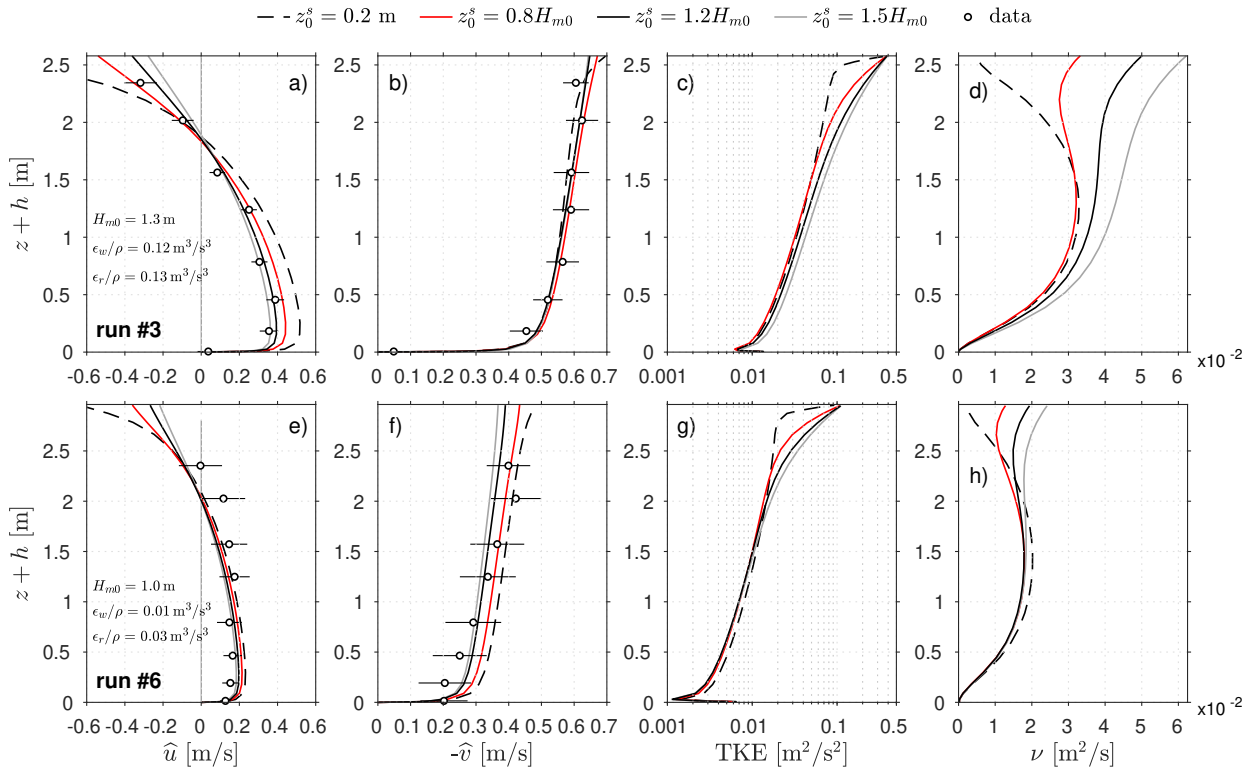
16

Figure 6: Sensitivity analysis of the simulated vertical distribution of $\hat{u}$ (a, e), $\hat{v}$ (b, f), TKE (c, g) and ν (d, h) to the surface mixing length z_0^s. The analysis is performed at the locations corresponding to sled run #3 (sandbar, upper panels) and #6 (trough region, lower panels). As in Fig. 5, error bars on observation data points represent one standard deviation of the 10-min window-averaged current velocities computed over the corresponding sled run. Additional relevant wave parameters are given in panels a) and e) for sled runs #3 and #6, respectively.

relatively large incidence angle, causing shear instabilities of the surf zone mean longshore current (*e.g.*, see Oltman-Shay et al., 1989; Noyes et al., 2004). The presence of wave groups, not represented in the present phase-averaged modelling approach, could also enhance the vertical mixing through their influence on the mean breakpoint cross-shore location (Symonds et al., 1982).

5. Analysis of wave setup dynamics during SandyDuck

In the previous Section, the modelling system SCHISM demonstrated excellent skills in reproducing the cross-shore transformation of directionally-broad waves and the associated depth-varying mean circulation in the surf zone. The predictions of wave setup computed with 2D-VF and 3D-VF approaches varied quite substantially during Duck94 (Fig. 4b), with differences ranging from 5-10% in the trough region and up to 25% closer to shore. However, the pressure data collected during this specific campaign did not allow the estimation of wave setup with sufficient accuracy for carefully verifying the present model's ability to reproduce it (Lentz and Raubenheimer, 1999). In this Section, our strategy is to use the data collected during the SandyDuck event described in Section 2.2 (13-14 November 1997, see Fig. 3) to study the wave setup dynamics at this site. As mentioned in Section 2.2, this event includes the largest underestimations of wave setup reported by Apotsos et al. (2007) at the shoreline with 2DH approaches based on Eq. 1.

The ability of the 3D-VF *baseline* configuration (see Section 4) to reproduce the cross-shore evolution of the wave setup is first assessed in Section 5.1 during both high- and low-tide situations (hereafter HT and LT, respectively). Two distinct 4h-long runs are performed for each case, with the final time step being used for the analysis (0:30AM for HT; 6:20PM for LT). The results obtained with the 3D-VF *baseline* configuration are compared with simulations performed in 2DH with both the Vortex-Force formalism (2D-VF) and the radiation stress formalism (2D-RS). Comparing 2D-3D configurations with the VF formalism helps quantifying by how much wave setup predictions can be improved when the depth-varying surf zone

17

circulation is resolved. The comparison with the 2D-RS configuration allows a comparison with common approaches in storm surge modelling at regional scales (*e.g.*, Dietrich et al., 2011), which is close to the approach used by Raubenheimer et al. (2001) for simulating the wave effects on currents near the shoreline. The accuracy of the modelling system for reproducing the wave setup cross-shore repartition during both HT and LT then allows us to analyse in Section 5.2 the contributions of the different terms in the momentum equations to the observed mean water elevations.

5.1. Model assessment for the 14 November event

In the surf zone, the wave forces associated with depth-induced breaking processes are the dominant forcing term for the wave setup and its cross-shore evolution (*e.g.*, see Guérin et al., 2018; Lavaud et al., 2022). It is thus essential to accurately reproduce the cross-shore evolution of wave heights in order to reduce as much as possible the bias in wave setup predictions owing to the wave forcing. During Duck94, the incident wave conditions estimated at the 8 m array allowed to describe the cross-shore evolution of significant wave heights with relative good accuracy (NRMSD between 6 and 10% depending on the tidal elevation, see Table 2). Since these errors were primarily explained by the two sensors located near the shoreline, this accuracy was sufficient for accurately reproducing the surf zone mean circulation and its vertical repartition (Fig. 5). This was not the case for the wave setup predictions during SandyDuck so that small calibrations were made to both the wave forcing taken from the 8 m array (see Section 2.3) and the wave breaking parametrisation: the default coefficient in the biphase definition of Eldeberky (1996) was adjusted to 0.19 (instead of 0.2) while the coefficient of the adaptive breaker parameter was adjusted to 45 (instead of 40, see Pezerat et al., 2021). With these adjustments, the cross-shore evolution of the significant wave heights could be reproduced with NRMSD $\lesssim$ 5% and almost no bias (normalised bias |NB| $\lesssim$ 2%) for both the HT and LT events (Fig. 7a and 7b, respectively).

On the 14 November 0:30AM (HT), H_{m0} reached 3 m at the 8 m array, corresponding to the storm peak (see Fig. 3b). Wave breaking already occurred at the most seaward wave gauge p72 ($x = 500$ m), and the gradual decrease of incident wave energy shown in Fig. 7a indicates that it never ceased until shore. The intensity of wave breaking processes is moderate up to $x \sim 300$ m, due to the mild slope, leading to a wave setup of around 5-6 cm around the trough region ($x = 250 - 300$ m). In contrast, wave breaking is weak over the same region during LT (Fig. 7b) due to the milder incident wave energy conditions, which led to a wave setup that did not exceed 1-2 cm (Fig. 7d). As incident short waves transitioned to the steeper section of the beach ($x = 150 - 225$ m, 1:30 beach slope), the intensity of wave breaking processes was more intense and associated with a rapid increase of the wave setup during both HT and LT (Fig. 7c and 7d, respectively). For both HT and LT situations, the 3D-VF approach better captures the cross-shore distribution of the wave setup, with NRMSD < 15% and |NB| $\lesssim$ 5% overall.

Representing the depth-varying nearshore circulation improves the wave setup predictions across the whole surf zone in both HT and LT situations (Fig. 7c and 7d). During LT, the predictions by the 2D-VF and 3D-VF configurations are nearly identical up to $x = 180$ m, where wave breaking becomes more intense and leads to increasing differences that reach their maximum at the shoreline (~15%), where the beach is the steepest (1:14 slope). In contrast, the wider surf zone during HT explains why differences between the 2D-VF and 3D-VF configurations are substantial up to $x = 250$ m. Over the rather steep region between $x = 160 - 250$ m, the wave setup predictions differ by 5-7%, explaining the improved NB obtained with the 3D-VF configuration overall. The wave setup predictions at the shoreline during HT are 11% smaller with the 2D-VF configuration compared to the 3D-VF one. Given the differences in terms of wave heights and periods during both situations, this tends to confirm the findings of Guérin et al. (2018) that differences in wave setup predictions at the shoreline between 2DH and 3D approaches are primarily controlled by the beach slope. Compared to the 2D-VF configuration, the wave setup predictions are strongly underestimated with the 2D-RS configuration: by 10-15% between $x = 200 - 300$ m during HT and by nearly 20% at the shoreline in both situations (30% compared to the 3D-VF). This can be explained by
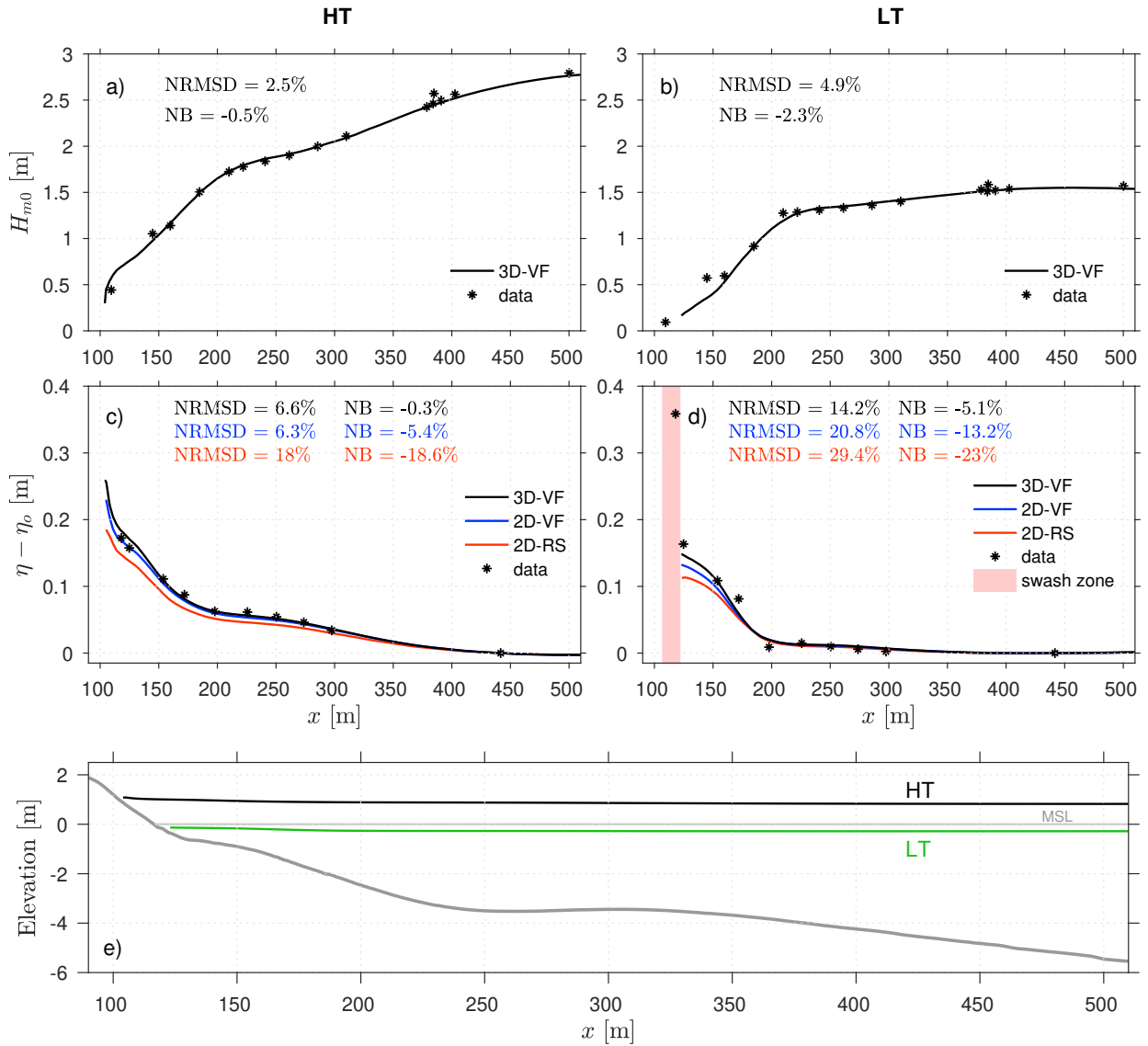
Figure 7: Assessment of the *baseline* 3D-VF configuration for simulating the cross-shore evolution of significant wave heights (a-b panels) and wave setup (c-d panels) during the high-tide (14 November 0:30AM; HT - left panels) and low-tide (14 November 6:20PM; LT - right panels) situations of the SandyDuck event considered here. The wave setup ($\eta - \eta_o$) is computed following Raubenheimer et al. (2001) and Apotsos et al. (2007) as the difference in the mean water surface elevation relative to q39 ($x \sim 445$ m). For LT, the red shaded region indicates the swash zone as identified in the phase-resolving SWASH simulations (see Appendix B). Panel e) shows the bathymetric profile relative to the MSL datum, along with the corresponding HT and LT mean water levels.

two main factors: 1) the cross-shore contribution from the bottom stress to the wave setup (Apotsos et al., 2007), which is ignored in 2D-RS modelling approaches but naturally included with the VF formalism, and 2) differences owing to potential limitations of the radiation stress concept to represent non-linear waves dynamics in the nearshore and in particular in the surf zone.

In Fig. 7d, the most landward data point at LT indicates a measured elevation relative to q39 of nearly 0.36 m, which is not reproduced by the model and is twice that measured around $x = 120$ m. Since this data point is also located in a region of the beach considered dry by the 3D-VF baseline configuration, with very little wave energy dissipation locally ($H_{m0} < 0.2$ m), there is no obvious physical explanation for this apparent underestimation of the wave setup at the shoreline with the present phase-averaged approach. An investigation of the LT situation with the phase-resolving SWASH model (see Appendix B) reveals that the most landward sensor was actually located within the swash zone. The data for this sensor hence contains swash oscillations, which cannot be represented with a phase-averaged approach. While resolving the depth-varying circulation with the VF formalism increases the prediction of the wave setup at the shoreline by 40-45% (*i.e.* the above-mentioned 30% difference) compared to a 2D-RS approach

19

at both HT and LT, this cannot explain the underestimations by up to a factor 2 reported by Raubenheimer et al. (2001) and Apotsos et al. (2007) in very shallow water depths. The difficulty in disentangling swash and wave motions close to the shoreline over steep foreshores in the field might provide an explanation for the remaining discrepancies between phase-averaged modelling approaches and field observations.

5.2. Analysis of the cross-shore momentum balance

For both HT and LT situations of the SandyDuck event considered here (Fig. 7c and 7d), the performance metrics obtained with the 3D-VF modelling approach are typically within the margin of errors in the observations (Raubenheimer et al., 2001). The slightly larger errors and bias obtained during LT can be explained by the underestimated setup around $x = 170$ m, which is also the case in the phase-resolving simulation (see Fig. B1). Adjusting the surface mixing length z_0^s to $1.5 H_{m0}$ (instead of $1.2 H_{m0}$ for the *baseline* model) improves the setup predictions at this specific location, but slightly deteriorates those at the shoreline. This spatial variation of the influence of vertical mixing on wave setup predictions (Bennis et al., 2014) might be explained by variations in breaking processes (*e.g.* breaking type varying between spilling and plunging) that are not incorporated in the present parametrisation of z_0^s. The absence of vertically-resolved current velocity measurements during SandyDuck prevents us to test this hypothesis further in the present study but it remains an interesting perspective. The accuracy of the wave predictions gives us great confidence for analysing the wave setup dynamics and the importance of accounting for the depth-varying surf zone circulation. The various contribution to the simulated wave setup can be analysed via a steady-state momentum balance in the cross-shore direction (Buckley et al., 2016; Guérin et al., 2018; Lavaud et al., 2022):

$$\frac{\partial \eta}{\partial x} = \frac{1}{gh} \int_{z_b}^{\eta} \left(-\hat{u}\frac{\partial \hat{u}}{\partial x} - \hat{v}\frac{\partial \hat{u}}{\partial y} - \hat{w}\frac{\partial \hat{u}}{\partial z} + \frac{\partial}{\partial z}\left(\nu\frac{\partial \hat{u}}{\partial z} \right) + F_x^{\mathrm{w}} \right) dz \tag{14}$$

where z_b is the seabed elevation and we remind that ν is the vertical eddy viscosity and F_x^{w} is the cross-shore component of the wave forces (see Eq. 6). The spatial derivatives of the terms on the right-hand side of Eq. 14 were evaluated using the shape functions of the unstructured grid finite elements (directly within the model), while we used simple finite differences for the vertical derivatives. The contribution of these terms to the simulated wave setup is then estimated by spatially-integrating the corresponding term along the cross-shore direction (Raubenheimer et al., 2001; Buckley et al., 2016; Guérin et al., 2018). For a consistent comparison with the data, the initial point is taken at the cross-shore location corresponding to q39 (see Fig. 3a). For instance, the contribution of the wave force η_{wafo} to the modelled wave setup at the cross-shore location x' is computed as:

$$\eta_{\mathrm{wafo}}(x') = \int_{x_{\mathrm{q39}}}^{x'} \int_{z_b}^{\eta(x)} \frac{F_x^{\mathrm{w}}}{gh(x)} dz dx \tag{15}$$

The contributions from the horizontal cross-shore ($\eta_{\hat{u}}$) and longshore ($\eta_{\hat{v}}$) advection terms, the vertical advection term ($\eta_{\hat{w}}$) and the vertical eddy viscosity term (η_ν) are computed similarly by spatially-integrating the corresponding term in Eq. 14. The relative contribution of a given term in % is then computed as 100 times this term divided by the sum of all contributions. Since the contribution from the alongshore advection was found negligible everywhere (< 0.3%), we neglect it hereafter. Before physically-interpreting these contributions, it should be noted that the depth-varying circulation in the surf zone is the result of a strong coupling between the intensity of breaking (major component of the wave forces in the surf zone), the parametrisation of the vertical mixing and the resulting cross-shore mean currents. Thus, these terms are still correlated to each other so that the individual contributions from depth-varying circulation terms ($\eta_{\hat{u}}$, $\eta_{\hat{v}}$, $\eta_{\hat{w}}$, η_ν) should be seen as an indicator of the improvement of wave setup predictions when the vertical is resolved.

Fig. 8a-b display the cross-shore evolution of the contributions to the wave setup from the different right-hand side terms of Eq. 14 for HT and LT, respectively, while their relative contribution (in %) is

20

shown in Fig. 8c-d. For both situations, the good match between the sum of the individual contributions and the setup simulated with the *baseline* 3D-VF approach indicates that the momentum balance closes well and each term was computed accurately. The wave forces explain more than 80% of the computed setup across the surf zone, but it is interesting to note that this contribution varies quite substantially in the cross-shore direction (by up to 20%). At HT, the relative contribution η_{wafo} decreases where the beach steepens (see between $x = 200 - 250\,\text{m}$ and $x = 100 - 140\,\text{m}$ in Fig. 8c), suggesting that the beach slope dependence of the wave setup reported in the literature (*e.g.*, see Bowen et al., 1968; Van Dorn, 1976) is related to the depth-varying surf zone circulation. The wave setup predictions in the 2D-VF configuration are mostly explained by the η_{wafo} relative contribution, with an additional contribution coming from the bottom shear stress. At the shoreline, where the beach is the steepest (1:14), the depth-varying circulation explains 18-20% of the computed wave setup, which is consistent with the results obtained over planar beaches by Guérin et al. (2018) and Lavaud et al. (2022). Among the depth-varying circulation terms, the vertical mixing term is dominant and accounts for 10-15% of the wave setup across the entire surf zone (Fig. 8c-d). The contribution from the vertical advection term becomes important on the steepest section of the beach and reaches 10% at the shoreline during HT. The horizontal advection term has a minor impact on the predictions of wave setup, which concentrates around regions where the energy dissipation rates vary strongly. The larger contribution of $\eta_{\hat{u}}$ found in Guérin et al. (2018) are likely explained by the cruder parametrisation used by these authors for the vertical mixing, which resulted in much more sheared currents (see also Fig. 6a for an example with insufficient breaking wave-induced mixing).

6. Concluding remarks and perspectives

Using a combination of field observations from past major campaigns (Duck94 and SandyDuck) and the application of a state-of-the-art phase-averaged 3D circulation modelling system, this study investigated the dynamics of wave setup on barred sandy beaches. A particular emphasis was given to quantifying
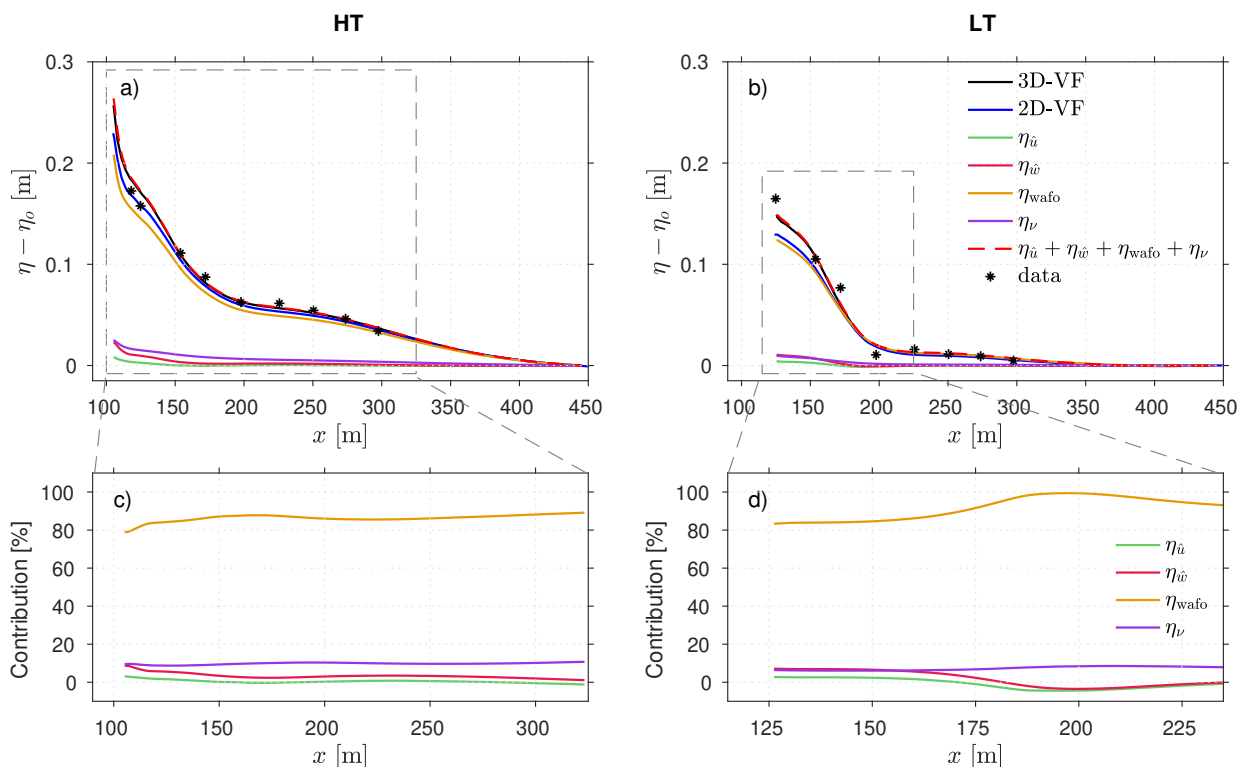

Figure 8: Contribution from the different right-hand side terms of Eq. 14 to the wave setup computed with the *baseline* configuration 3D-VF for HT (a) and LT (b), respectively. Their relative contribution (in %) is shown in panels c) and d) over a reduced spatial region for HT and LT, respectively. As mentioned previously, the wave setup ($\eta - \eta_o$) is computed following Raubenheimer et al. (2001) and Apotsos et al. (2007) as the difference in the mean water surface elevation relative to q39 ($x \sim 445\,\text{m}$).

how much resolving the depth-varying surf zone circulation can impact and improve the predictions of wave setup, especially close to the shoreline. The traditional benchmark of Duck94 (sled experiments of the 12 October 1994, see Garcez Faria et al., 1998, 2000) was first revisited, and used to assess the ability of the modelling system SCHISM to reproduce the depth-varying surf zone circulation during the ∼ 9 h that spanned the sled experiments. A sensitivity analysis of the mean cross-shore currents to the surface mixing length z_0^s revealed that the vertical shear is strongly controlled by the choice of z_0^s, whose parametrisation remains quite empirical and could focus research efforts in the future.

The wave setup dynamics was then studied using the data collected during the SandyDuck campaign (Raubenheimer et al., 2001; Apotsos et al., 2007). Slight adjustments made to the parametrisation of wave breaking processes helped improving the match between observed and modelled significant wave heights. This improved representation of the wave energy dissipation by breaking, and its cross-shore distribution, eventually led to very accurate predictions of wave setup across the whole beach profile with our *baseline* 3D-VF configuration (NRMSD < 15%, |NB| ≲ 5%). A comparison with a 2D-VF configuration confirmed the findings of Guérin et al. (2018): accounting for the depth-varying surf zone circulation significantly increases and improves the predictions of wave setup across the surf zone, with a 10 − 15% difference at the shoreline on the steep foreshore during Sandyduck (slope in 1:14). Simulations during the Duck94 campaign suggest that this difference can reach 25% on slightly steeper foreshores (slope in 1:12), when more wave energy can reach the shoreline (see Fig. 4). Though all terms from the 3D cross-shore momentum balance are clearly coupled, an analysis of their individual contribution to the simulated wave setup revealed that the vertical mixing was the second most important contributor (10-15% across the surf zone) after the wave forces (80-90%), followed by the vertical advection whose contribution increases with the beach slope (up to 10% at the shoreline). Overall, this study highlights the need to represent wave processes and the resulting depth-varying circulation at high-resolution near complex shorelines in order to accurately reproduce the associated mean water levels and flooding risks. When 3D approaches are not possible, the VF formalism should still be preferred over the traditional 2DH approach based on the radiation stresses, for two principal reasons: 1) by resolving $\hat{u}$ instead of u^l, the equations of motions naturally incorporates the cross-shore contribution from the bottom shear stress to the wave setup, and 2) the decomposition of the conservative and non-conservative forces (mostly breaking) removes uncertainties associated with the estimation of radiation stresses in the surf zone based on linear wave theory.

Finally, the improvements obtained with the 3D-VF approach were not sufficient to explain the underestimation of the wave setup close to shore by up to a factor of 2 that are reported in Raubenheimer et al. (2001) and Apotsos et al. (2007) with common 2DH radiation stress-based approaches (closely equivalent to our 2D-RS configuration). Such severe underestimations only occur at the location of the pressure sensor closest to shore (q29) during low tides. A phase-resolving numerical experiment revealed that this sensor was most probably located in the swash region, and was thus affected by swash motions. Identifying this discrepancy not only reveals the difficulty in measuring the wave setup close the shoreline on steep beaches, but it underlines the need to further develop the capacity of phase-averaged modelling approaches to predict extreme water levels at the shoreline. Indeed, phase-averaged models fully-coupled to oceanic circulation modelling systems play a critical role in operational applications or in early-warning systems worldwide (help for other references Khan et al., 2021). In this context, the present findings suggest that modelling approaches relying on the Vortex-Force formalism (either 2D or 3D) should be preferred over the radiation stress-based approach for improved predictions of water levels along wave-exposed coastlines. Interesting perspectives also exist for incorporating swash statistics into phase-averaged models in order to develop the capacity for these modelling systems to predict wave runup and hence extreme water levels during storm conditions.

Appendix A: Forcing terms for the quasi-Eulerian velocities

Let us recall that the wave action density spectrum $N(\sigma, \theta)$ is related to the wave energy density spectrum $E(\sigma, \theta)$ by $N = E/\sigma$. In the following, the expressions for the different terms composing the wave forcing term $\mathbf{F}^{\mathrm{w}}$ are described.

For random waves, the Stokes drift horizontal velocities can be expressed as:

$$\mathbf{u}^{\mathrm{st}}(z) = \int\limits_{0}^{2\pi} \int\limits_{0}^{\infty} \sigma E(\sigma, \theta) \frac{\cosh(2k(\sigma)(z + h))}{\sinh^2(k(\sigma)(\eta + h))} \mathbf{k}\, d\sigma d\theta \tag{16}$$

where $k(\sigma)$ is the wavenumber determined from the linear wave dispersion relation and $\mathbf{k} = k(\sigma)\,(\cos\theta, \sin\theta)$ (Bennis et al., 2011). At lowest order, the Stokes drift flow is non-divergent (Ardhuin et al., 2008) so that the three components of the Stokes drift velocities verify:

$$\nabla \cdot \mathbf{u}^{\mathrm{st}} + \frac{\partial w^{\mathrm{st}}}{\partial z} = 0 \tag{17}$$

In practice, the vertical component w^{st} of the Stokes drift velocities is retrieved from the divergence of $\mathbf{u}^{\mathrm{st}}$ following Bennis et al. (2011):

$$w^{\mathrm{st}}(z') = -u^{\mathrm{st}}(-h)\frac{\partial h}{\partial x} - v^{\mathrm{st}}(-h)\frac{\partial h}{\partial y} + \int\limits_{z_b}^{z'} \nabla \cdot \mathbf{u}^{\mathrm{st}}\, dz \tag{18}$$

where z' is any elevation between the seabed elevation z_b and the free surface elevation η.

The other conservative forcing term is the depth-homogeneous wave-induced pressure term, defined as follows (Bennis et al., 2011):

$$J = \int\limits_{0}^{2\pi} \int\limits_{0}^{\infty} g \frac{E(\sigma, \theta)}{\sinh(2k(\sigma)(\eta + h))} k(\sigma)\, d\sigma d\theta \tag{19}$$

Appendix B: Estimation of the wave runup with a phase-resolving model

The strong underestimation of the wave setup (roughly a factor 2) identified at the shoreline during low-tides (q29 sensor, see at $x \sim 118$ m in Fig. 7d) is quite common in the 3 month-long dataset of Apotsos et al. (2007). This underestimation remained unexplained until now and the improved representation of the wave setup with the present 3D-VF numerical approach (by $\sim 30\%$ at the shoreline) is not sufficient to explain this discrepancy. Considering the fairly accurate representation of the wave setup between $x = 120$-170 m (mean water depth < 1.3 m), the observed behaviour indicates the possible influence of swash-related processes. In order to investigate this further, we applied a phase-resolving model (SWASH) to the low-tide situation of 14 November 6:20PM.

The non-hydrostatic model SWASH (Zijlema et al., 2011) solves the Reynolds-averaged Navier-Stokes equations for an incompressible, constant-density fluid with a free surface (the free surface elevation is here noted ζ in order to differentiate it from the phase-averaged value used above). The ability of the SWASH model to reproduce the nearshore wave transformation, and the resulting wave setup and runup has been extensively assessed with data collected in both laboratory (Smit et al., 2014; Rijnsdorp et al., 2014; de Bakker et al., 2016) and field conditions (Nicolae-Lerma et al., 2017; Fiedler et al., 2018). We here performed 2DV simulations with 4 layers in the vertical and a horizontally uniform grid resolution of 0.2 m. The forcing consisted of JONSWAP spectra fitted to the sea-surface spectra observed at the 8 m array (the spectral shape factor γ was adjusted to 5, instead of the default value of 3.3). For the bottom friction, a Manning's roughness coefficient of 0.015 was set while the α and μ parameters for the hydrostatic front approximation (HFA; Smit et al., 2013) for simulating wave breaking onset were adjusted to 0.55 and 2, respectively. Simulations are run for 130 min and the first 10 min were discarded from the present analysis.

The instantaneous shoreline is defined as the most seaward grid point with a water depth lower than 1 cm. The most seaward location reached by the instantaneous shoreline defines the beginning of the swash zone. The time-varying shoreline position directly informs on the swash vertical excursion ς, which is used to estimate $R_{2\%}$, the 2% exceedence value of runup, following Stockdon et al. (2006):

$$R_{2\%} = 1.1 \left(<\zeta> + 2\sqrt{<(\varsigma - <\varsigma>)^2>} \right) \tag{20}$$

where $< \, . \, >$ is the time-averaging operator (the free surface elevation here fluctuates at the scale of individual waves). Fig. B1a compares the observed and simulated significant wave heights for short waves and confirms the capacity of the numerical model to accurately simulate the cross-shore transformation of short waves across the shoaling and breaking wave regions. Fig. B1b compares the resulting wave setup simulated with SWASH against the observations. Consistent with the observations, the simulated wave setup $<\zeta> - <\zeta_o>$ was here estimated as the difference in the mean water surface elevation relative to q39 ($x \sim 445$ m). The wave setup is accurately reproduced, though a small underestimation is evident at the fourth sensor, located at $x = 170$ m (as with the phase-averaged approach, see Section 5.1). For the LT situation simulated here, the swash zone initiates between the first two sensors, and extends up to $x \sim 100$ m. In contrast with the phase-averaged approach of SCHISM (Section 5.1), the SWASH model resolves swash motions, and a good match is obtained with the wave setup observed at $x = 118$ m.
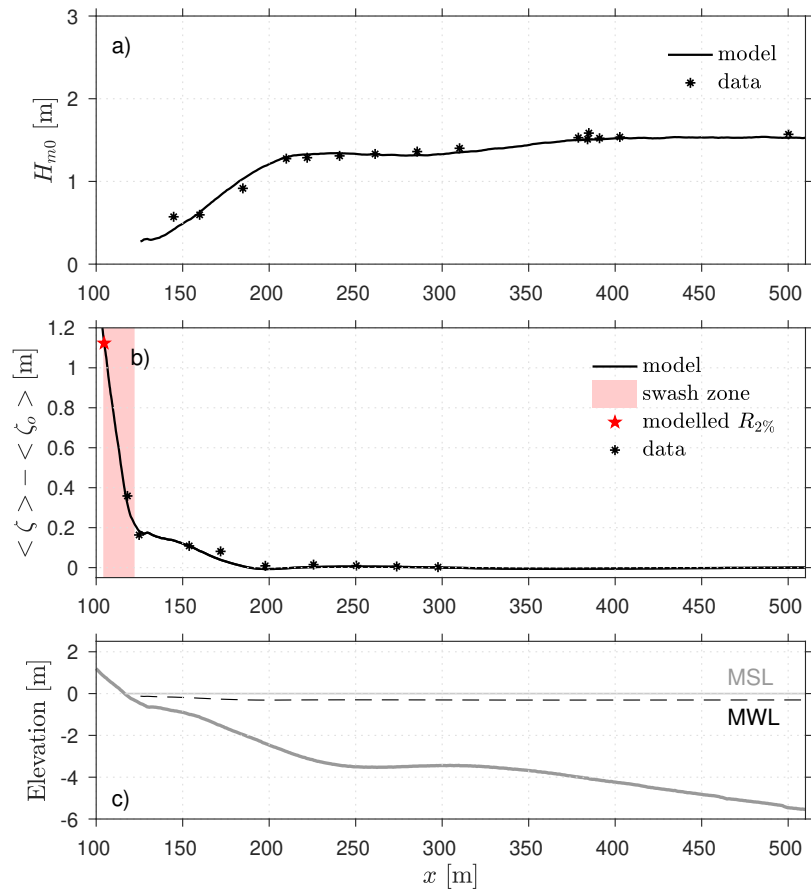
Figure B1: Results from the SWASH simulations during the LT situation during the SandyDuck campaign (14 November 6PM).

References

Abgrall, R., 2006. Residual distribution schemes: Current status and future trends. Computational Fluids 35, 641 – 669. doi:10.1016/j.compfluid.2005.01.007.

Andrews, D.G., McIntyre, M.E., 1978. An exact theory of nonlinear waves on a Lagrangian-mean flow. Journal of Fluid Mechanics 89, 609 – 646. doi:10.1017/S0022112078002773.

Apotsos, A., Raubenheimer, B., Elgar, S., Guza, R.T., Smith, J.A., 2007. Effects of wave rollers and bottom stress on wave setup. Journal of Geophysical Research: Oceans 112. doi:10.1029/2006JC003549.

Ardhuin, F., Herbers, T.H.C., Jessen, P.F., O'Reilly, W.C., 2003. Swell transformation across the continental shelf. Part II: Validation of a spectral energy balance equation. Journal of Physical Oceanography 33, 1940 – 1953. doi:10.1175/1520-0485(2003)033<1940:STATCS>2.0.CO;2.

Ardhuin, F., Rascle, N., Belibassakis, K.A., 2008. Explicit wave-averaged primitive equations using a generalized lagrangian mean. Ocean Modelling 20, 35 – 60. doi:10.1016/j.ocemod.2007.07.001.

Ardhuin, F., Rogers, E., Babanin, A.V., Filipot, J.F., Magne, R., Roland, A., van der Westhuysen, A., Queffeulou, P., Lefevre, J.M., Aouf, L., Collard, F., 2010. Semiempirical dissipation source functions for ocean waves. Part I: Definition, calibration, and validation. Journal of Physical Oceanography 40, 1917 – 1941. doi:10.1175/2010JPO4324.1.

de Bakker, A.T.M., Tissier, M.F.S., Ruessink, B.G., 2016. Beach steepness effects on nonlinear infragravity-wave interactions: A numerical study. Journal of Geophysical Research: Oceans 121, 554 – 570. doi:10.1002/2015JC011268.

Bennis, A.C., Ardhuin, F., Dumas, F., 2011. On the coupling of wave and three-dimensional circulation models: Choice of theoretical framework, practical implementation and adiabatic tests. Ocean Modelling 40, 260 – 272. doi:10.1016/j.ocemod.2011.09.003.

Bennis, A.C., Dumas, F., Ardhuin, F., Blanke, B., 2014. Mixing parameterization: Impacts on rip currents and wave set-up. Ocean Engineering 84, 213 – 227. doi:10.1016/j.oceaneng.2014.04.021.

Bertin, X., Fortunato, A.B., Oliveira, A., 2009. A modeling-based analysis of processes driving wave-dominated inlets. Continental Shelf Research 29, 819 – 834. doi:10.1016/j.csr.2008.12.019.

Birkemeier, W., Long, C., Hathaway, K., 1996. DELILAH, DUCK94 & SandyDuck: Three nearshore field experiments, in: Proceedings of the 25th Conference on Coastal Engineering, Orlando, Florida, pp. 4052 – 4065.

Blumberg, A.F., Mellor, G.L., 1987. A Description of a Three-Dimensional Coastal Ocean Circulation Model. American Geophysical Union (AGU). pp. 1 – 16. doi:10.1029/CO004p0001.

Bonneton, P., Bruneau, N., Castelle, B., Marche, F., 2010. Large-scale vorticity generation due to dissipating waves in the surf zone. Discrete & Continuous Dynamical Systems - B 13, 729 – 738. doi:10.3934/dcdsb.2010.13.729.

Bowen, A.J., Inman, D.L., Simmons, V.P., 1968. Wave 'set-down' and set-up. Journal of Geophysical Research (1896-1977) 73, 2569 – 2577. doi:10.1029/JB073i008p02569.

Bretschneider, C.L., Krock, H.J., Nakazaki, E., Casciano, F.M., 1986. Roughness of typical Hawaiian terrain for tsunami run-up calculations: A users manual. J. K. K. Look Laboratory report, Univ. of Hawaii, Honolulu, Hawaii.

Buckley, M.L., Lowe, R.J., Hansen, J.E., Dongeren, A.R.V., 2016. Wave setup over a fringing reef with large bottom roughness. Journal of Physical Oceanography 46, 2317–2333. doi:10.1175/JPO-D-15-0148.1.

Bühler, O., Jacobson, T.E., 2001. Wave-driven currents and vortex dynamics on barred beaches. Journal of Fluid Mechanics 449, 313–339. doi:10.1017/S0022112001006322.

Burchard, H., 2001. Simulating the wave-enhanced layer under breaking surface waves with two-equation turbulence models. Journal of Physical Oceanography 31, 3133–3145. doi:10.1175/1520-0485(2001)031<3133:STWELU>2.0.CO;2.

Castelle, B., Scott, T., Brander, R.W., McCarroll, R.J., 2016. Rip current types, circulation and hazard. Earth-Science Reviews 163, 1–21. doi:10.1016/j.earscirev.2016.09.008.

Craig, P.D., Banner, M.L., 1994. Modeling wave-enhanced turbulence in the ocean surface layer. Journal of Physical Oceanography 24, 2546–2559. doi:10.1175/1520-0485(1994)024<2546:MWETIT>2.0.CO;2.

de Beer, A.F., McCall, R.T., Long, J.W., Tissier, M.F.S., Reniers, A.J.H.M., 2021. Simulating wave runup on an intermediate–reflective beach using a wave-resolving and a wave-averaged version of xbeach. Coastal Engineering 163, 103788. doi:10.1016/j.coastaleng.2020.103788.

Deconinck, H., Ricchiuto, M., 2007. Residual Distribution Schemes: Foundations and Analysis. Encyclopedia of Computational Mechanics, John Wiley & Sons, Ltd. doi:10.1002/0470091355.ecm054.

Deigaard, R., 1993. A note on the three-dimensional shear stress distribution in a surf zone. Coastal Engineering 20, 157–171. doi:10.1016/0378-3839(93)90059-H.

Deigaard, R., Fredsøe, J., 1989. Shear stress distribution in dissipative water waves. Coastal Engineering 13, 357–378. doi:10.1016/0378-3839(89)90042-2.

Deigaard, R., Justesen, P., Fredsøe, J., 1991. Modelling of undertow by a one-equation turbulence model. Coastal Engineering 15, 431–458. doi:10.1016/0378-3839(91)90022-9.

Delpey, M.T., Ardhuin, F., Otheguy, P., Jouon, A., 2014. Effects of waves on coastal water dispersion in a small estuarine bay. Journal of Geophysical Research: Oceans 119, 70–86. doi:10.1002/2013JC009466.

Dietrich, J.C., Zijlema, M., Westerink, J.J., Holthuijsen, L.H., Dawson, C., Luettich, R.A., Jensen, R.E., Smith, J.M., Stelling, G.S., Stone, G.W., 2011. Modeling hurricane waves and storm surge using integrally-coupled, scalable computations. Coastal Engineering 58, 45–65. doi:10.1016/j.coastaleng.2010.08.001.

Duncan, J.H., 1981. An experimental investigation of breaking waves produced by a towed hydrofoil. Proceedings of the Royal Society A 377, 331–348. doi:10.1098/rspa.1981.0127.

Eldeberky, Y., 1996. Nonlinear transformations of wave spectra in the nearshore zone. Ph.D. thesis. Delft University of Technology, Delft.

Eldeberky, Y., Battjes, J.A., 1996. Spectral modeling of wave breaking: Application to boussinesq equations. Journal of Geophysical Research: Oceans 101, 1253–1264. doi:10.1029/95JC03219.

Elgar, S., Guza, R.T., Raubenheimer, B., Herbers, T.H.C., Gallagher, E.L., 1997. Spectral evolution of shoaling and breaking waves on a barred beach. Journal of Geophysical Research: Oceans 102, 15797–15805. doi:10.1029/97JC01010.

Fairchild, J.C., 1958. Model study of wave set-up induced by hurricane waves at Narragansett Pier. The Bulletin of the Beach Erosion Board, U.S. Army Corps of Engineers, Washington, D.C. .

Feddersen, F., 2012. Observations of the surf-zone turbulent dissipation rate. Journal of Physical Oceanography 42, 386–399. doi:10.1175/JPO-D-11-082.1.

Feddersen, F., Trowbridge, J.H., 2005. The effect of wave breaking on surf-zone turbulence and alongshore currents: A modeling study. Journal of Physical Oceanography 35, 2187−2203. doi:10.1175/JPO2800.1.

Fiedler, J.W., Brodie, K.L., McNinch, J.E., Guza, R.T., 2015. Observations of runup and energy flux on a low-slope beach with high-energy, long-period ocean swell. Geophysical Research Letters 42, 9933−9941. doi:10.1002/2015GL066124.

Fiedler, J.W., Smit, P.B., Brodie, K.L., McNinch, J., Guza, R.T., 2018. Numerical modeling of wave runup on steep and mildly sloping natural beaches. Coastal Engineering 131, 106−113. doi:10.1016/j.coastaleng.2017.09.004.

Fortunato, A.B., Freire, P., Bertin, X., Rodrigues, M., Ferreira, J., Liberato, M.L., 2017. A numerical study of the february 15, 1941 storm in the tagus estuary. Continental Shelf Research 144, 50−64. doi:10.1016/j.csr.2017.06.023.

Garcez Faria, A.F., Thornton, E.B., Lippmann, T.C., Stanton, T.P., 2000. Undertow over a barred beach. Journal of Geophysical Research: Oceans 105, 16999−17010. doi:10.1029/2000JC900084.

Garcez Faria, A.F., Thornton, E.B., Stanton, T.P., Soares, C.V., Lippmann, T.C., 1998. Vertical profiles of longshore currents and related bed shear stress and bottom roughness. Journal of Geophysical Research: Oceans 103, 3217−3232. doi:10.1029/97JC02265.

Garrett, C., 1976. Generation of langmuir circulations by surface waves—a feedback mechanism. Journal of Marine Research 34, 117−130.

Gomes, E.R., Mulligan, R.P., Brodie, K.L., McNinch, J.E., 2016. Bathymetric control on the spatial distribution of wave breaking in the surf zone of a natural beach. Coastal Engineering 116, 180−194. doi:10.1016/j.coastaleng.2016.06.012.

Guérin, T., Bertin, X., Coulombier, T., de Bakker, A., 2018. Impacts of wave-induced circulation in the surf zone on wave setup. Ocean Modelling 123, 86−97. doi:10.1016/j.ocemod.2018.01.006.

Guza, R.T., Thornton, E.B., 1981. Wave set-up on a natural beach. Journal of Geophysical Research: Oceans 86, 4133−4137. doi:10.1029/JC085iC03p01524.

Hargreaves, J.C., Annan, J.D., 2001. Comments on "improvement of the short-fetch behavior in the Wave Ocean Model (WAM)". Journal of Atmospheric and Oceanic Technology 18, 711−715. doi:10.1175/1520-0426(2001)018<0711:COIOTS>2.0.CO;2.

Hasselmann, S., Hasselmann, K., Allender, J.H., Barnett, T.P., 1985. Computations and parameterizations of the nonlinear energy transfer in a gravity-wave specturm. part ii: Parameterizations of the nonlinear energy transfer for application in wave models. Journal of Physical Oceanography 15, 1378−1391. doi:10.1175/1520-0485(1985)015<1378:CAPOTN>2.0.CO;2.

Huang, Z.C., Hsiao, S.C., Hwung, H.H., Chang, K.A., 2009. Turbulence and energy dissipations of surf-zone spilling breakers. Coastal Engineering 56, 733−746. doi:10.1016/j.coastaleng.2009.02.003.

Khan, M.J.U., Durand, F., Bertin, X., Testut, L., Krien, Y., Islam, A.K.M.S., Pezerat, M., Hossain, S., 2021. Towards an efficient storm surge and inundation forecasting system over the bengal delta: chasing the supercyclone amphan. Natural Hazards and Earth System Sciences 21, 2523−2541. doi:10.5194/nhess-21-2523-2021.

Komen, G.J., Cavaleri, L., Donelan, M., Hasselmann, K., Hasselmann, S., Janssen, P.A.E.M., 1994. Dynamics and Modelling of Ocean Waves. Cambridge University Press, Cambridge, U.K. doi:10.1017/CBO9780511628955.

Kumar, N., Voulgaris, G., Warner, J.C., Olabarrieta, M., 2012. Implementation of the vortex force formalism in the coupled ocean-atmosphere-wave-sediment transport (COAWST) modeling system for inner shelf and surf zone applications. Ocean Modelling 47, 65–95. doi:10.1016/j.ocemod.2012.01.003.

Lavaud, L., Bertin, X., Martins, K., Arnaud, G., Bouin, M.N., 2020. The contribution of short-wave breaking to storm surges: The case Klaus in the Southern Bay of Biscay. Ocean Modelling 156, 101710. doi:10.1016/j.ocemod.2020.101710.

Lavaud, L., Bertin, X., Martins, K., Pezerat, M., Coulombier, T., Dausse, D., 2022. Wave dissipation and mean circulation on a shore platform under storm wave conditions. Journal of Geophysical Research: Earth Surface 127, e2021JF006466. doi:10.1029/2021JF006466.

Leibovich, S., 1980. On wave-current interaction theories of langmuir circulations. Journal of Fluid Mechanics 99, 715–724. doi:10.1017/S0022112080000857.

Lentz, S., Raubenheimer, B., 1999. Field observations of wave setup. Journal of Geophysical Research: Oceans 104, 25867–25875. doi:10.1029/1999JC900239.

Long, C.E., 1996. Index and bulk parameters for frequency-direction spectra measured at CERC Field Research Facility, June 1994 to August 1995. Miscellaneous Paper CERC-96-6, US Army Corps of Engineers Waterways Experiment Station.

Longuet-Higgins, M.S., Stewart, R.W., 1962. Radiation stress and mass transport in gravity waves, with application to 'surf beats'. Journal of Fluid Mechanics 13, 481–504. doi:10.1017/S0022112062000877.

Longuet-Higgins, M.S., Stewart, R.W., 1964. Radiation stresses in water waves; a physical discussion, with applications. Deep Sea Research and Oceanographic Abstracts 11, 529–562. doi:10.1016/0011-7471(64)90001-4.

Malhadas, M.S., Leitão, P.C., Silva, A., Neves, R., 2009. Effect of coastal waves on sea level in Óbidos lagoon, portugal. Continental Shelf Research 29, 1240–1250. doi:10.1016/j.csr.2009.02.007.

Martins, K., Blenkinsopp, C.E., Deigaard, R., Power, H.E., 2018. Energy dissipation in the inner surf zone: New insights from lidar-based roller geometry measurements. Journal of Geophysical Research: Oceans 123, 3386–3407. doi:10.1029/2017JC013369.

Martins, K., Bonneton, P., Lannes, D., Michallet, H., 2021. Relation between orbital velocities, pressure, and surface elevation in nonlinear nearshore water waves. Journal of Physical Oceanography 51, 3539–3556. doi:10.1175/JPO-D-21-0061.1.

McWilliams, J.C., Restrepo, J.M., Lane, E.M., 2004. An asymptotic theory for the interaction of waves and currents in coastal waters. Journal of Fluid Mechanics 511, 135–178. doi:10.1017/S0022112004009358.

Michallet, H., Cienfuegos, R., Barthélemy, E., Grasso, F., 2011. Kinematics of waves propagating and breaking on a barred beach. European Journal of Mechanics - B/Fluids 30, 624–634. doi:10.1016/j.euromechflu.2010.12.004.

Michaud, H., Marsaleix, P., Leredde, Y., Estournel, C., Bourrin, F., Lyard, F., Mayet, C., Ardhuin, F., 2012. Three-dimensional modelling of wave-induced current from the surf zone to the inner shelf. Ocean Science 8, 657–681. doi:10.5194/os-8-657-2012.

Moghimi, S., Klingbeil, K., Gräwe, U., Burchard, H., 2013. A direct comparison of a depth-dependent radiation stress formulation and a vortex force formulation within a three-dimensional coastal ocean model. Ocean Modelling 70, 132–144. doi:10.1016/j.ocemod.2012.10.002.

Moghimi, S., Thomson, J., Özkan Haller, T., Umlauf, L., Zippel, S., 2016. On the modeling of wave-enhanced turbulence nearshore. Ocean Modelling 103, 118 – 132. doi:10.1016/j.ocemod.2015.11.004.

Morgan, S.G., Shanks, A.L., MacMahan, J.H., Reniers, A.J.H.M., Feddersen, F., 2018. Planktonic subsidies to surf-zone and intertidal communities. Annual Review of Marine Science 10, 345 – 369. doi:10.1146/annurev-marine-010816-060514.

Newberger, P.A., Allen, J.S., 2007a. Forcing a three-dimensional, hydrostatic, primitive-equation model for application in the surf zone: 1. Formulation. Journal of Geophysical Research: Oceans 112. doi:10.1029/2006JC003472.

Newberger, P.A., Allen, J.S., 2007b. Forcing a three-dimensional, hydrostatic, primitive-equation model for application in the surf zone: 2. Application to DUCK94. Journal of Geophysical Research: Oceans 112. doi:10.1029/2006JC003474.

Nicolae-Lerma, A., Pedreros, R., Robinet, A., Sénéchal, N., 2017. Simulating wave setup and runup during storm conditions on a complex barred beach. Coastal Engineering 123, 29 – 41. doi:10.1016/j.coastaleng.2017.01.011.

Nielsen, P., 1988. Wave setup: A field study. Journal of Geophysical Research: Oceans 93, 15643 – 15652. doi:10.1029/JC093iC12p15643.

Noyes, T.J., Guza, R.T., Elgar, S., Herbers, T.H.C., 2004. Field observations of shear waves in the surf zone. Journal of Geophysical Research: Oceans 109. doi:10.1029/2002JC001761.

Olabarrieta, M., Warner, J.C., Kumar, N., 2011. Wave-current interaction in willapa bay. Journal of Geophysical Research: Oceans 116. doi:10.1029/2011JC007387.

Oltman-Shay, J., Howd, P.A., Birkemeier, W.A., 1989. Shear instabilities of the mean longshore current: 2. Field observations. Journal of Geophysical Research: Oceans 94, 18031 – 18042. doi:https://doi.org/10.1029/JC094iC12p18031.

Peregrine, D.H., Bokhove, O., 1998. Vorticity and surf zone currents, in: Proceedings of the 26th Conference on Coastal Engineering, Copenhagen, Denmark, pp. 745 – 748.

Pezerat, M., Bertin, X., Martins, K., Lavaud, L., 2022. Cross-shore distribution of the wave-induced circulation over a dissipative beach under storm wave conditions. Journal of Geophysical Research: Oceans 127, e2021JC018108. doi:10.1029/2021JC018108.

Pezerat, M., Bertin, X., Martins, K., Mengual, B., Hamm, L., 2021. Simulating storm waves in the nearshore area using spectral model: Current issues and a pragmatic solution. Ocean Modelling 158, 101737. doi:10.1016/j.ocemod.2020.101737.

Phillips, O.M., 1977. The dynamics of the upper ocean. volume 2 of *Cambridge Monographs on Mechanics and Applied Mathematics*. Cambridge University Press.

Raubenheimer, B., Guza, R.T., Elgar, S., 2001. Field observations of wave-driven setdown and setup. Journal of Geophysical Research: Oceans 106, 4629–4638. doi:10.1029/2000JC000572.

Reniers, A.J.H.M., Roelvink, J.A., Thornton, E.B., 2004. Morphodynamic modeling of an embayed beach under wave group forcing. Journal of Geophysical Research: Oceans 109. doi:10.1029/2002JC001586.

Rijnsdorp, D.P., Smit, P.B., Zijlema, M., 2014. Non-hydrostatic modelling of infragravity waves under laboratory conditions. Coastal Engineering 85, 30 – 42. doi:10.1016/j.coastaleng.2013.11.011.

Roland, A., 2009. Development of WWM II: Spectral wave modeling on unstructured meshes. Ph.D. thesis. Institute of Hydraulic and Water Resources Engineering, Technical University of Darmstadt, Darmstadt, Germany.

Roland, A., Zhang, Y.J., Wang, H.V., Meng, Y., Teng, Y.C., Maderich, V., Brovchenko, I., Dutour-Sikiric, M., Zanke, U., 2012. A fully coupled 3D wave-current interaction model on unstructured grids. Journal of Geophysical Research: Oceans 117. doi:10.1029/2012JC007952.

Savage, R.P., 1957. Model tests for hurricane protection project. The Bulletin of the Beach Erosion Board, U.S. Army Corps of Engineers .

Saville, T., 1961. Experimental determination of wave set-up, in: Proceedings of the Second Technical Conference on Hurricanes, p. 242.

Smit, P., Janssen, T., Holthuijsen, L., Smith, J., 2014. Non-hydrostatic modeling of surf zone wave dynamics. Coastal Engineering 83, 36 – 48. doi:10.1016/j.coastaleng.2013.09.005.

Smit, P., Zijlema, M., Stelling, G., 2013. Depth-induced wave breaking in a non-hydrostatic, near-shore wave model. Coastal Engineering 76, 1 – 16. doi:10.1016/j.coastaleng.2013.01.008.

Smith, J.A., 2006. Wave-current interactions in finite depth. Journal of Physical Oceanography 36, 1403 – 1419. doi:10.1175/JPO2911.1.

Soulsby, R.L., 2005. Bed shear-stresses due to combined waves and currents. In: Stive, M., Fredsøe, J., Hamm, L., Soulsby, R., Teisson, C., Winterwerp, J., Advances in Coastal Morphodynamics. Delft Hydraulics, Delft, The Netherlands. pp. 420 – 423.

Stive, M.J.F., de Vriend, H.J., 1994. Shear stresses and mean flow in shoaling and breaking waves, in: Proceedings of the 24th Conference on Coastal Engineering, Kobe, Japan, pp. 594 – 608.

Stive, M.J.F., Wind, H.G., 1982. A study of radiation stress and set-up in the nearshore region. Coastal Engineering 6, 1 – 25. doi:10.1016/0378-3839(82)90012-6.

Stive, M.J.F., Wind, H.G., 1986. Cross-shore mean flow in the surf zone. Coastal Engineering 10, 325 – 340. doi:10.1016/0378-3839(86)90019-0.

Stockdon, H.F., Holman, R.A., Howd, P.A., Sallenger, A.H., 2006. Empirical parameterization of setup, swash, and runup. Coastal Engineering 53, 573 – 588. doi:10.1016/j.coastaleng.2005.12.005.

Svendsen, I.A., 1984a. Mass flux and undertow in a surf zone. Coastal Engineering 8, 347 – 365. doi:10.1016/0378-3839(84)90030-9.

Svendsen, I.A., 1984b. Wave heights and set-up in a surf zone. Coastal Engineering 8, 303 – 329. doi:10.1016/0378-3839(84)90028-0.

Symonds, G., Huntley, D.A., Bowen, A.J., 1982. Two-dimensional surf beat: Long wave generation by a time-varying breakpoint. Journal of Geophysical Research: Oceans 87, 492 – 498. doi:10.1029/JC087iC01p00492.

Terray, E.A., Donelan, M.A., Agrawal, Y.C., Drennan, W.M., Kahma, K.K., Williams, A.J., Hwang, P.A., Kitaigorodskii, S.A., 1996. Estimates of kinetic energy dissipation under breaking waves. Journal of Physical Oceanography 26, 792 – 807. doi:10.1175/1520-0485(1996)026<0792:EOKEDU>2.0.CO;2.

Ting, F.C., Kirby, J.T., 1995. Dynamics of surf-zone turbulence in a strong plunging breaker. Coastal Engineering 24, 177 – 204. doi:10.1016/0378-3839(94)00036-W.

Uchiyama, Y., McWilliams, J.C., Shchepetkin, A.F., 2010. Wave-current interaction in an oceanic circulation model with a vortex-force formalism: Application to the surf zone. Ocean Modelling 34, 16 – 35. doi:10.1016/j.ocemod.2010.04.002.

Umlauf, L., Burchard, H., 2003. A generic length-scale equation for geophysical turbulence models. Journal of Marine Research 61, 235 – 265. doi:10.1357/002224003322005087.

Van Dorn, W.G., 1976. Set-up and run-up in shoaling breakers, in: Proceedings of the 15th Conference on Coastal Engineering, Honolulu, Hawaii, pp. 738 – 751.

Walstra, D.J.R., Roelvink, J.A., Groeneweg, J., 2000. Calculation of wave-driven currents in a 3d mean flow model, in: Proceedings of the 27th Conference on Coastal Engineering, Sydney, Australia, pp. 1050 – 1063. doi:10.1061/40549(276)81.

van der Westhuysen, A.J., 2010. Modeling of depth-induced wave breaking under finite depth wave growth conditions. Journal of Geophysical Research: Oceans 115. doi:10.1029/2009JC005433.

Wilcox, D.C., 1988. Reassessment of the scale-determining equation for advanced turbulence models. AIAA Journal 26, 1299 – 1310. doi:10.2514/3.10041.

Wright, L.D., Short, A.D., 1984. Morphodynamic variability of surf zones and beaches: A synthesis. Marine Geology 56, 93 – 118. doi:10.1016/0025-3227(84)90008-2.

Zhang, Y.J., Baptista, A.M., 2008. SELFE: A semi-implicit Eulerian-Lagrangian finite-element model for cross-scale ocean circulation. Ocean Modelling 21, 71 – 96. doi:10.1016/j.ocemod.2007.11.005.

Zhang, Y.J., Ye, F., Stanev, E.V., Grashorn, S., 2016. Seamless cross-scale modeling with SCHISM. Ocean Modelling 102, 64 – 81. doi:10.1016/j.ocemod.2016.05.002.

Zheng, L., Weisberg, R.H., Huang, Y., Luettich, R.A., Westerink, J.J., Kerr, P.C., Donahue, A.S., Crane, G., Akli, L., 2013. Implications from the comparisons between two- and three-dimensional model simulations of the hurricane ike storm surge. Journal of Geophysical Research: Oceans 118, 3350 – 3369. doi:10.1002/jgrc.20248.

Zheng, P., Li, M., van der A, D.A., van der Zanden, J., Wolf, J., Chen, X., Wang, C., 2017. A 3D unstructured grid nearshore hydrodynamic model based on the vortex force formalism. Ocean Modelling 116, 48 – 69. doi:10.1016/j.ocemod.2017.06.003.

Zijlema, M., Stelling, G., Smit, P., 2011. SWASH: An operational public domain code for simulating wave fields and rapidly varied flows in coastal waters. Coastal Engineering 58, 992 – 1012. doi:10.1016/j.coastaleng.2011.05.015.